Multi-Dimensional Quantitative Laser-based Diagnostics - Development and Practial Applications

Wellander, Rikard

2014

Multi-Dimensional Quantitative Laser-based Diagnostics

Development and Practial Applications

Doctoral Thesis

Rikard Wellander

Division of Combustion Physics
Department of Physics

LUND 2014

LUND
UNIVERSITY

Printed by: Media-Tryck, Lund, Sweden
November 2014

Lund Reports on Combustion Physics, LRCP-177
ISSN 1102-8718
ISRN LUTFD2/TFCP-177-SE
ISBN (print) 978-91-7623-203-3
ISBN (pdf) 978-91-7623-204-0

Rikard Wellander
Division of Combustion Physics
Department of Physics
Lund University
P.O. Box 118
SE-221 00, Lund, Sweden

If the picture is worth a thousand words
a movie must be worth a fortune
and this thesis is priceless

Abstract

Laser based optical diagnostic methods are routinely used in combustion research. Many of the more common approaches are based on illuminating a cross-section of the sample with a thin laser sheet. For example, by targeting an electronic transition in a molecule, its concentration within the plane illuminated by the laser sheet can be deduced. By probing the relative occurrence of an atom or molecule in different rotational or vibrational states or by probing the Doppler shift in Rayleigh scattering, it is possible to extract the temperature. The flow field can be measured by seeding particles into the measurement volume and following them through multiple exposures. The work reported in the thesis concerns the development, improvement and applications of measurement techniques based on laser sheet illumination.

The aforementioned techniques are most often employed on a single shot basis, providing independent snapshots of two-dimensional (2D) data. In some examples, the measurement techniques are extended to the third spatial dimension, and in resent years, studies employing high repetition rate measurements capable of resolving the dynamics in time have become more frequent. In the thesis, a method for simultaneously extending the measurements to the third spatial dimension and to the time dimension, is presented. A high repetition rate laser and detection system is combined with oscillating mirrors, the laser sheet being scanned back and forth throughout the measurement volume. The deflections from two mirrors operated at different frequencies are combined to obtain equidistant laser sheets in the measurement region. The method is demonstrated on the Mie-scattering from a flow of droplets and is used to probe the planar laser induced fluorescence (PLIF) from the OH in a flame. Post processing methods to calculate concentrations and flame-fronts from large data sets are demonstrated.

Measurements of droplet concentration and size distribution in sprays, based on recording the light scattered from a laser sheet, suffer from uncertainties due to multiple scattering (MS) and attenuation of the illuminating and scattered light. A method is demonstrated here, that takes advantage of the ability to suppress the MS light by means of structured illumination. After MS suppression, the attenuation of the laser and signal light can be compensated for by comparing the transmission through the spray with the side-scattered signal. In the process, the local extinction coefficient is calculated from the Beer-Lambert law.

Laser based optical diagnostic techniques are in general developed for atmospheric flames under ideal laboratory conditions. In the application of the same techniques in more realistic situations, such as internal combustion (IC) engines, the harsh conditions involving vibrations, varying pressure, moving parts, limited optical access and a sooty environment have to be taken into account. Several of the measurement campaigns reported in the thesis were conducted in IC engines. Although the main goals of these campaigns were to answer combustion or engine related questions, time has also been invested in improving and adopting the measurement techniques to the existing conditions. By following the spray propagation in a light duty-diesel engine over time, knowledge was gained regarding how early spray injections should be conducted to avoid wall wetting. From high speed laser induce incandescence (LII) measurements in a heavy-duty Diesel engine, conclusions regarding soot formation and oxidation were drawn. The implementation of LII at high repetition rates in IC engines was investigated here. Challenges associated with attenuation of the laser and signal light were also addressed. Visualization of the flame jet propagation in a large-bore gas engine was made possible by means of fuel tracer LIF. Apart from the combustion related conclusions, it was shown that the image quality could be improved substantially by the use of correction optics.

Populärvetenskaplig Sammanfattning

De vanligaste anledningarna till att vi eldar idag är att skapa värme, elektricitet eller mekanisk energi (som till exempel i bilar och andra fordon). När man eldar bildas kemikalier och partiklar som är skadliga för hälsa och miljö. För att minimera mängden av dessa skadliga utsläpp och för att optimera mängden energi som man kan utvinna från en viss mängd bränsle, är det viktigt att man förstår vad som händer i flamman. För att skaffa denna förståelse behöver man kunna mäta storheter som temperatur, hastigheten på gasflödena och koncentration av olika kemikalier och partiklar. Informationen från mätningarna kan, förutom att öka förståelsen för hur förbränningen påverkas av olika yttre omständigheter, användas för att förbättra noggrannheten i datormodeller utvecklade för att förutsäga förbränningsprocessen. Informationen kan också användas för att lösa tekniska problem som uppstår i specifika förbränningssammanhang.

Det går så klart att samla in information från flamman med hjälp av fysiska mätinstrument, som till exempel termoelement för att mäta temperatur. Problemet med dessa är de i sig påverkar flamman så att de storheter som mäts ändras. Ett termoelement påverkar till exempel gasflödet, kan agera som katalysator för vissa kemiska reaktioner och kyler lokalt gasen i flamman. Den temperatur som mäts blir då annorlunda än vad den varit om inget termoelement stört flamman. Ett vanligt sätt att samla in information från en flamma, utan att påverka den, är att istället fotografera den med en kamera. Som ljuskälla används i regel en kort laserpuls, formad till ett tunt laserark (istället för blixt som används vid vanlig fotografering). Att använda ett laserark som ljuskälla jämfört med att detektera det ljus som naturligt strålar ut från flamman, har flera fördelar. Dels kan laserarket göras så kort att inget hinner hända i flamman under exponeringen. Man får alltså en bild av hur det är under just tidpunkten då laserarket passerar istället för en suddig medelvärdesbild av vad som händer under kamerans exponeringstid (som att fotografera något som rör sig snabbt med eller utan blixt). Dessutom kommer ljuset, som detekteras av kameran, bara från det område som laserarket belyser, alltså en skarp genomskärning istället för ett medelvärde från hela djupet av flamman. Men den största fördelen är nog ändå att man genom att justera färgen på laserljuset kan välja vilken typ av information som bilden kommer innehålla. Många av molekylerna som finns i flamman reagerar bara på vissa specifika färger. Genom att välja ett laserljus med en färg som överensstämmer med den molekyl man är intresserad av får man en signal som innehåller information om fördelningen av detta ämne i genomskärningen av flamman. Man kan även välja att anpassa laserljusets färg för att se hur snabbt molekylerna vibrerar och roterar, och med denna information räkna ut temperaturen i flamman. Vill man veta flödeshastigheterna – alltså hur snabbt och i vilken riktning

gasen rör sig i varje punkt i flamman – kan man tillsätta små partiklar, belysa dessa med två laserark efter varandra och se hur långt partiklarna flyttat sig under tiden mellan exponeringarna.

Historiskt sett har den utrustning som använts för att fotografera i flammorna (lasrarna och kamerorna) kunnat användas med en uppdateringsfrekvens på ett tiotal bilder per sekund. Under tiden mellan två bilder har det då hunnit hända så mycket att det inte längre går att säga om de är tagna direkt efter varandra eller med längre tid emellan. I den här avhandlingen har en relativt ny typ av laser och kamerautrustning använts, som kan användas med flera tusen exponeringar per sekund. På så sätt kan man studera vad som händer i flamman över tiden och inte bara hur läget är vid en specifik tidpunkt. Lite som att spela in en film istället för att ta stillbilder. Dessutom har en teknik utvecklats där laserarket hastigt skannas fram och tillbaka i flamman. På så sätt kan information från alla tre rumsliga dimensioner samlas in och resultatet blir en 3D-film.

Det finns mycket att göra för att förbättra mätmetoderna utöver att utöka dom till fler dimensioner. För att mätningarna ska ha hög noggrannhet krävs till exempel att man vet hur många fotoner (ljuspartiklar) som befinner sig i laserarket. Fotonernas antal kan dock ändra sig med tiden, då de sprids eller absorberas av partiklarna och molekylerna i mätvolymen. Det spridda ljuset, som normalt skulle registreras av kameran, kan också absorberas eller spridas innan det kommit fram till kameran. Båda de ovan nämnda effekterna ger upphov till att mindre ljus registreras och det finns risk att datan feltolkas. Det finns också en risk att redan spridda fotoner sprids en eller flera gånger till, så kallad multipelspridning. Multipelspridningarna kan ske från positioner som ligger utanför laserarket och därmed ge upphov till en falsk signal. I den här avhandlingen demonstreras en metod som kan kompensera för ovan nämnda fel. För att särskilja det multipelspridda ljuset från det som bara spridits en gång introduceras ett randmönster i laserarket. De fotoner som sprids flera gånger förlorar randstrukturen och kan på matematisk väg särskiljas från de som bara spridits en gång och därmed har randmönstret bevarat. När de multipelspridda fotonerna rensats bort beter sig dämpningen av ljuset i laserarket och den spridda signalen på ett matematiskt förutsägbart sätt. Från den detekterade signalen som kommer från ett visst område i mätvolymen, kan man därmed räkna ut hur mycket ljuset dämpats i detsamma område. Den informationen kan då användas för att räkna ut den faktiska mängden fotoner i den intilliggande mätvolymen och på så sätt kan man undvika felet som dämpningen av signalen annars skulle gett upphov till där.

Mycket av arbetet som rapporteras i avhandlingen har alltså handlat om att utveckla nya mätmetoder. Men det är en sak att en mätmetod fungerar i en öppen mätvolym i en laboratoriemiljö, och en helt annan sak att få det att fungera tillfredsställande i praktiska sammanhang, som i förbränningsmotorer. Avhandlingen behandlar även mätningar gjorda i förbränningsmotorer. Dessa mätningarna och analyserna av dom har lett till: Ökad förståelse för hur sot bildas och oxideras i en dieselmotor, hur man kan lösa problemet med att bränslesprayen träffar cylinderväggen vid tidig insprutning av bränsle i små dieselmotorer och hur jetflamman utvecklas och tänder gasen i en gasmotor med förkammartändning. Under dessa mätningar har en rad utmaningar kopplade till mätningar i förbränningsmotorer stötts på och antagits. Ett exempel på en sådan utmaning är de optiska fel som skapas när ljuset bryts

i de krökta fönster[1] som sitter i motorn. Optik och mjukvara har utvecklats som kompenserar för dessa fel, som annars hade lett till suddiga och förvrängda bilder. Ett annat exempel är att en diagnostikmetod som inriktar sig på att detektera sot har undersökts med hänseende till hur den påverkas av att användas i tidsupplösta mätningar i en förbränningsmotor.

Sammanfattningsvis har forskningen resulterat i att en diagnostisk metod tagits fram för att öka noggrannheten i mätningar genom att kompensera för dämpningen och multipelspridningen av ljuset i mätvolymen. En mätmetod har demonstrerats som möjliggör tidsupplösta mätningar i 3D. Mätmetoder har anpassats för att kunna mäta i de mer krävande miljöer som skapas inne i förbränningsmotorer. Datan från de sistnämnda mätningarna har analyserats och lett till en ökad förståelse kring vissa processer i diesel- och gasmotorer.

[1] För att kunna se in i motorn byter man ut en del av metallen i t.ex. cylindern eller kolvkronan mot kvartsglas. För att inte ändra på förbränningsrummets utformning formas dessa fönster likadant som de krökta ytorna i cylinderväggen/kolvkronan.

List of Papers

The thesis is based on the papers that are appended to the thesis in the order listed here.

I. **Wellander, R.**, Richter, M., and Aldén, M., "Time resolved, 3D imaging (4D) of two phase flow at a repetition rate of 1 kHz," Optics Express **19**, 21508-21514 (2011).

II. **Wellander, R.**, Richter, M., and Aldén, M., "Time-resolved (kHz) 3D imaging of OH PLIF in a flame," Experiments in Fluids **55**, 1-12 (2014).

III. **Wellander, R.**, Berrocal, E., Kristensson, E., Richter, M., and Aldén, M., "Three-dimensional measurement of the local extinction coefficient in a dense spray," Measurement Science & Technology **22** (2011).

IV. Lequien G., A. Ö., Johansson B., **Wellander, R.**, Rosell J., Richter M, Aldén M., "Liquid Spray Penetration Length during Late Post Injection in an Optical Light-Duty Diesel Engine," Comodia 8th, CI-10 (2012).

V. Sjöholm, J., **Wellander, R.**, Bladh, H., Richter, M., Bengtsson, P.-E., Aldén, M., Aronsson, U., Chartier, C., Andersson, Ö., and Johansson , B., "Challenges for In-Cylinder High-Speed Two-Dimensional Laser-Induced Incandescence Measurements of Soot" SAE international journal of engines **4**, 1607-1622 (2011).

VI. Aronsson, U., Chartier, C., Andersson, Ö., Johansson, B., Sjöholm, J., **Wellander, R.**, Richter, M., Aldén, M., and Miles, P., "Analysis of EGR Effects on the Soot Distribution in a Heavy Duty Diesel Engine using Time-Resolved Laser Induced Incandescence," SAE international journal of engines **3**, 137-155 (2010).

VII. **Wellander, R.**, Rosell, J., Richter, M., Aldén, M., Andersson, Ö., Johansson, B., Duong, J., and Hyvonen, J., "Study of the Early Flame Development in a Spark-Ignited Lean Burn Four-Stroke Large Bore Gas Engine by Fuel Tracer PLIF," SAE International Journal of Engines **7**, 928-936 (2014).

Related Work

A. Kristensson, E., Berrocal, E., **Wellander, R.**, Ritcher, M., Aldén, M., and Linne, M., "Structured illumination for 3-D Mie imaging and 2-D attenuation measurements in optically dense sprays," Proceedings of the Combustion Institute **33**, 855-861 (2011).

B. Petersson, P., **Wellander, R.**, Olofsson, J., Carlsson, H., Carlsson, C., Watz, B. B., Boetkjaer, N., Richter, M., Aldén, M., and Fuchs, L., "Simultaneous high-speed PIV and OH PLIF measurements and modal analysis for investigating flame-flow interaction in a low swirl flame," in 16th Int Symp on Applications of Laser Techniques to Fluid Mechanics, (Lisbon, Portugal, 2012).

C. Duong, J., **Wellander, R.**, Hyvönen, J., Andersson, Ö., Richter, M., Johansson, B., and Aldén, M., "High Speed Combustion Imaging in a Large Bore Gas Engine: The Relationship Between Pre-and Main Chamber Heat Release," in ASME 2013 International Mechanical Engineering Congress and Exposition, (American Society of Mechanical Engineers, 2013).

Abbreviations

2D	Two-dimensional
3D	Three-Dimensional
ADC	Analog-to-Digital Converter
CAD	Crank Angle Degrees
CCD	Charge-Coupled Device
CMOS	Complementary Metal-Oxide-Semiconductor
CW	Continuous Wave
IC	Internal Combustion
LIF	Laser-Induced Fluorescence
LII	Laser Induced Incandescence
LSS	Laser Sheet Scanning
MCP	Micro-Channel Plate
MS	Multiple Scattering
NURBS	Non-Uniform Rational B-Splines
PDA	Phase Doppler Anemometry
PIV	Particle Image Velocimetry
PLIF	Planar LIF
PSF	Point Spread Function
RMS	Root Mean Square
rpm	revolutions per minute
S/N	Signal-to-Noise-ratio
SLIPI	Structured Laser Illumination Planar Imaging
DPSS	Diode Pumped Solid State

Contents

Chapter 1

Introduction

With the emission of greenhouse gases, whereof CO_2 is the main contributor, human beings have managed to influence the climate in a manner leading to increasing global temperatures, reduction in the ice and snow coverage, higher sea levels and more frequent extreme weather conditions, as probable results of it [1]. Of the total energy consumption in the world, some 81 % has its origin in the combustion of fossil fuels [2]. Although the energy contribution of renewable resources is increasing, the extraction of fossil-based fuels is expected to continue to increase in the near future [3].

In the combustion of hydrocarbon species, the main chemical products are water and carbon dioxide. However, even in a modern controlled combustion environment it is inevitable that residuals of soot particles together with nitrogen oxides, sulfur oxides and/or partially or unburned hydrocarbons, are emitted in the combustion process. Such emissions have negative effect on our health, primarily through increasing the risk of respiratory and cardiovascular diseases [4]. Also, the local environment is affected by the increase in smog and acidification.

Although most companies set aside the environmental considerations in favor of increasing profit, customer demand for lower fuel consumption and the enforcement of ever more stringent constraints in global and local emission regulations forces them to direct effort at this area. Historically, improvements in combustion technology have been based primarily on a trial and error approach, small changes in a combustion system being made, the efficiency and the emission of it being monitored. However, in order to be able to effectively reduce emissions while at the same time maintaining high efficiency in energy conversion, it is important to understand the combustion process. The invention of lasers and development of computers in the sixties opened up possibilities for measuring what is really going on and for constructing models able to simulate what certain changes in variables should do to the combustion taking place. Since then, numerous laser-based experimental methods capable of measuring concentrations, fluid flows, and temperatures have been developed and been refined over the years [5]. Ideally, it would be possible to fully model combustion processes and thereby be able to predict the impact of different variables so as to be able to optimize the combustion environment without expensive and time-consuming hardware modifications. However, the interaction between the millions of chemical pathways that are

present in the combustion of hydrocarbons together with the complex fluid dynamics and heat transfer processes accompanying it, makes such an approach computationally inaccessible. To enable modeling of relevant combustion processes to be carried out with the limited computational power available, approximations have to be made. In order to validate the models and determine their limitations, it is essential to be able to accurately measure temperatures, concentrations, particle size-distributions and fluid flow fields.

Until the computational models have been validated to the extent that they can be regarded as trustworthy under non-tested conditions, optical diagnostic techniques will be important not only for model validation, but also for the testing of scientific hypotheses, so as to obtain knowledge of the combustion processes involved and for solving specific engineering problems. The development of new optical diagnostic techniques is relevant for all of the aforementioned applications. In Fig. 1.1 the various branches of combustion science that have been mentioned are depicted schematically. The papers upon which the thesis is based are placed within their proper context in the figure.

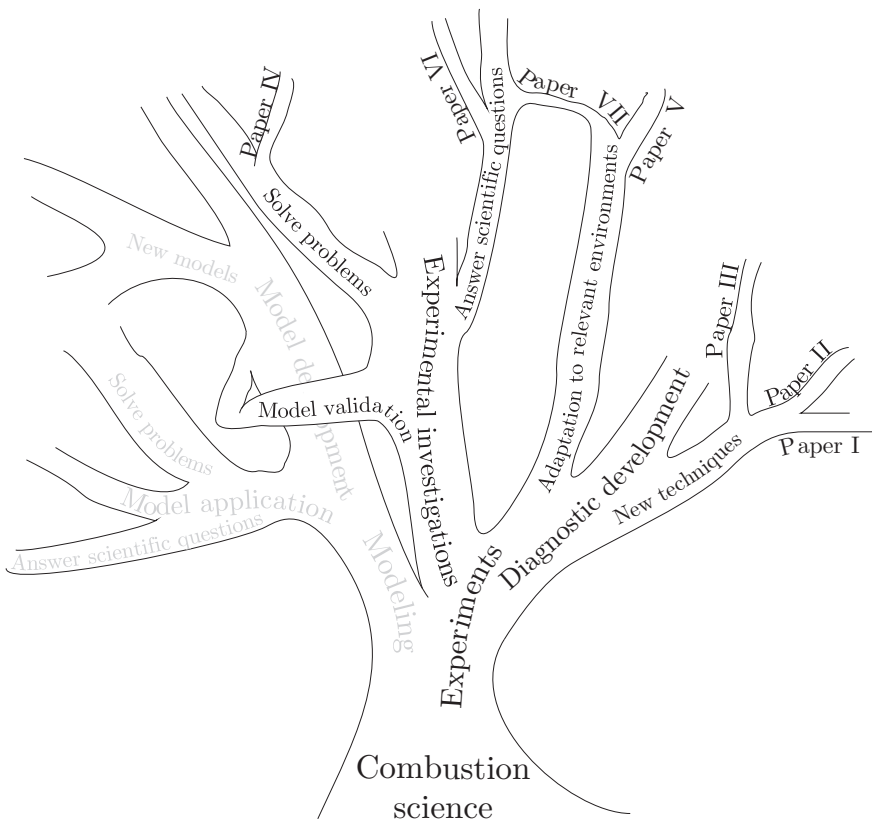

Figure 1.1: *Schematic picture of the different scientific directions to be found within combustion science. The papers constituting the basis of the thesis are placed in their respective context.*

With sufficiently high repetition rates in laser systems and in detectors, it is possible to monitor temporal processes in the reactive flows involved. Many of the investigations reported in the thesis (Papers I, II, IV, V and VI), are based on such time-resolved measurements, and Chapter 2 is thus devoted to high repetition rate combustion diagnostics. Chapter 3 is concerned with the extension of time-resolved imaging to the third spatial dimension, as dealt with in Papers I and II. Chapter 4 deals with efforts at quantifying measurements in turbid media, which is also the focus of Paper III. In Chapter 5 challenges associated with applying established techniques in internal combustion (IC) engines, taken up in Papers V, VI and VII, are discussed.

Chapter 2

High Repetition Rate

EVER since the first laser-based optical diagnostics studies in flames were conducted in the early 80:s [6], Q-switched Neodymium lasers operating at around 10 Hz have been the most common source of illumination. In such investigations, each recording is statistically independent of the others, the recordings as a whole thus being well suited for calculating the statistical quantities, such as means and variances, that can be used for model validation. However, for studying the dynamics of reactive flows, such as spray/jet propagation, mixture preparation, flame/flow interactions, acoustic instabilities, extinction/ignition and stabilization, the use of time-resolved measurements made at sufficiently high repetition rates to resolve the dynamics of the flow, are required [7]. In this section, the lasers and detection systems used for time-resolved laser based combustion diagnostics are described, with emphasis being placed on the methods employed in the work reported in the thesis.

2.1 Lasers

The lack of powerful high-repetition lasers has been a major limiting factor for time-resolved (high repetition rate) imaging studies of reactive flows. Early studies suggested excimer or copper vapor lasers to be used for such experiments [8]. However, the relatively low repetition rates or pulse energy of such lasers limit their use to the investigations of slow events or to use in combination with imaging techniques such as Mie scattering having a high signal yield [9]. Accordingly, the first time-resolved measurements in reactive flows based on laser sheet imaging involved use of laser clusters. In a laser cluster the outputs from several identical 10-Hz systems are overlapped spatially and are synchronized temporally to the predetermined time separation [10, 11].

2.1.1 Laser clusters

The main advantage in the use of clustered laser systems as compared with other high repetition rate systems is that the former are based on the same technology as the mature 10-Hz laser systems are. Thus, with decades of technical improvements and advancement, properties such as good beam quality, stability and high fluence comes

for free. Also, since the laser pulses originate from different lasers, the time distance between two pulses does not affect the beam characteristics and is only limited by the laser pulse length and the time jitter in the system.

The main drawback with use of laser clusters is probably that the number of laser pulses in a burst train is limited by the number of lasers that are combined in the cluster. The highest number of combined lasers reported in the literature is four, which operated in double pulse mode can provide a pulse train consisting of eight pulses [10]. Adding more lasers rapidly adds to the costs and complexity involved. Thus, although the temporal distance between laser pulses can be set to be sufficiently short to target the highest turbulence or to be sufficiently long to follow slower dynamics, these two goals cannot be achieved simultaneously, the temporal dynamic range available thus being low. A second drawback concerns difficulties in combining spatially the laser beams from the individual lasers involved. Commonly, this problem is solved in the frequency-doubling process. The fundamental laser output from the first laser is frequency converted to a shorter wavelength and is combined with the fundamental from the second laser by use of a dichroic mirror. In the non-linear crystal used to frequency-convert the second laser beam, the first laser beam passes by essentially unaffected. The procedure is repeated thereafter until all the laser beams overlap each other at the new wavelength. The overall procedure just described has been employed with use of up to four double-pulsed lasers (eight laser shots) [10], and is also employed in Paper V.

2.1.2 Diode pumped solid state lasers

In recent years, Diode Pumped Solid State (DPSS) lasers have become powerful enough to be a viable alternative in high repetition rate two-dimensional (2D) combustion diagnostics. Instead of using a flash lamp as pump source, as in conventional 10-Hz systems and laser clusters, the active medium is pumped by a diode array. With a narrow spectral profile of the diode emission, the conversion to laser light can be more efficient than in a flash lamp pumped system, with less waste heat generated in the process. This, in combination with the continuous nature of the diode pumping, allows for a three to four order of magnitude higher repetition rates and for continuously operated systems, as compaed with flash lamp pumped equivalents. The main advantage in the use of DPSS laser systems is their ability to operate continuously at relatively high (~10 kHz) repetition rates, this enabling the capture of both slow and fast events simultaneously. Also, the continuous operation enables one to capture rare events such as flame extinction. The main drawback is the limited pulse fluence and the sensitivity of the beam characteristics to the repetition rate. In addition, at high repetition rates the energy profile becomes unstable and may require pulse-to-pulse monitoring.

2.1.3 Pulsed burst lasers

A third approach for the creation of pulsed laser light at a high repetition rate, one that deserves to be mentioned (despite its not being utilized in the work covered by the thesis), is that of pulsed burst laser systems [12]. In these laser system, the laser light originates from a stable continuous wave (CW) laser that is chopped up by a Pockels cell into a burst of pulses of the desired pulse length and repetition

rate. The weak pulse train is amplified then in several amplification stages until the desired pulse energy has been reached. The pulse energy can be comparable to that provided by laser clusters. The repetition rate is in the order of 100 kHz and the burst duration is limited to tens of milliseconds [13]. The length of the pulse burst increases as the technique is improved and the flash-lamp amplifiers are replaced by the corresponding diode-based versions. The obvious drawbacks of systems of this sort are that the technique is immature and expensive, one that up until recently was not available commercially. Problems in maintaining a constant fluence and a constant spatial laser profile during the pulse burst are also difficult.

2.2 Detectors

The detection systems that can be used have evolved in parallel with the lasers in question, different solutions being suitable for different laser systems. In digital detectors the incident photons excite electrons over the potential gap in the semiconductors that produce each pixel. For long, the type of detector most commonly used in research have been based on charged-coupled devices (CCDs). In these detectors the readout of the voltage is managed by shifting the potentials from pixel to pixel until they reach the common analog to digital converter (ADC). The frame rate is thus limited by the rate of the ADC and by the number of pixels to be read. Usually the frame rate on scientific CCD cameras is around 10 Hz, its thus being well suited for 10 Hz laser systems but not as useful in high repetition rate applications. To circumvent this problem, so-called framing cameras have been developed.

2.2.1 Framing cameras

Framing cameras have the common property that the readout is too slow for the desired repetition rate. Instead of reading out the image after each exposure, multiple images are recorded and are read out together when all of them have been exposed. There are two types of framing cameras. In the one type, part of the CCD-chip is covered by a mask, the potentials in the unmasked pixels being transfered rapidly to masked pixels during the periods between the exposures [14]. In a second type, the light is split and is imaged on as many CCD-chips as there are frames available. Each chip has an exposure timing then corresponding to the desired timing of each frame. In the former case the resolution is reduced since only $1/n_{max}$ of the pixels are active, where n_{max} corresponds to the maximum number of successive frames that can be recorded prior to readout. In the latter case, the signal-to-noise ratio (S/N) is reduced since only $1/n_{max}$ of the light reaches each CCD-chip. A framing camera of the latter kind was used in Paper V.

2.2.2 CMOS cameras

Complementary metal-oxide-semiconductor (CMOS) sensors are named after the circuitry that sits on each pixel and that enables amplification and direct readout row-by-row by separate ADCs. With parallel readout, the frame rate can be increased by a factor corresponding to the number of rows in the sensor. The fastest high speed cameras on the market at the time of publication of the thesis have a frame rate of

around 20000 frames per second (fps). Thus they are well suited for measurements in connections with use of DPSS lasers.

The main drawback of high speed CMOS cameras is that each pixel has its own background and gain. In addition, these properties vary with temperature and with camera settings. There are "scientific" CMOS cameras on the market in which the temperature is well controlled and the difference in background and gain is minimized and is compensated for. However, these versions have not yet reached the high-speed segment, and until then one has to characterize each detector and compensate then for any flaws in the post processing of the data. In addition the cameras should be given sufficient time to stabilize in temperature (a matter which varies between cameras) and dark field images should be recorded in order to compensate for any offset which is present [15].

2.3 Image intensifiers

The image intensifier is an ad-on to the detector, used whenever the detector on its own is incapable of distinguishing the signal from the background light. In the context of laser-based combustion diagnostics, the two most common reasons for use of an image intensifier are to shift the wavelength of the light to within the sensitive spectral range of the detector and to achieve short exposure times in order to suppress a high-level constant background. Thus, an image intensifier is used whenever UV light is to be detected and/or when the constant background can be rejected by the time gating of a short signal pulse.

The basic principle of an image intensifier is shown in Fig. 2.1. The first part, in which the incident photons are detected, is the photocathode. When photons that exceed the work function of the material in the photocathode are absorbed, electrons are ejected. These electrons retain the distribution of the incident photons – i.e. of the image projected on the photocathode – as they are accelerated across an electric field to the next part of the image intensifier, the micro-channel plate (MCP). In each channel of the MCP, the electrons are accelerated in a variable electric field of up to ~1000V. Each time an electron collides with the wall in one of the channels, a bunch of new electrons are released. This continues throughout the channel in an exponential manner, until the electron bunch reaches the end of the MCP, were it is accelerated over several thousands Volts directed at a phosphor screen. The phosphor is excited by the energetic electrons and phosfluoresces with an intensity pattern proportional to that projected on the photocatode, but much brighter. In high speed imaging a second *booster stage*, consisting of an extra photocathode and a phosphor screen, are often added so as to further boost the signal (not shown in Fig. 2.1).

There are certain disadvantages associated with use of an image intensifier. Accordingly, whenever use of it is not required – i.e. when the signal light is in the visible range and the background light level is low – then it is better to omit its use. The most obvious disadvantage of use of it is probably the reduced resolution it results in. As the electron bunch propagates between the MCP and the phosphor screen it is spread out, due to the electrostatic repulsion between the individual electrons. As a result, the information from each photon that is detected is spread out over a larger area, the resolution thus being decreased. To reduce this effect, the voltage gain in the MCP can be reduced. For lower gain levels, each electron bunch contains fewer

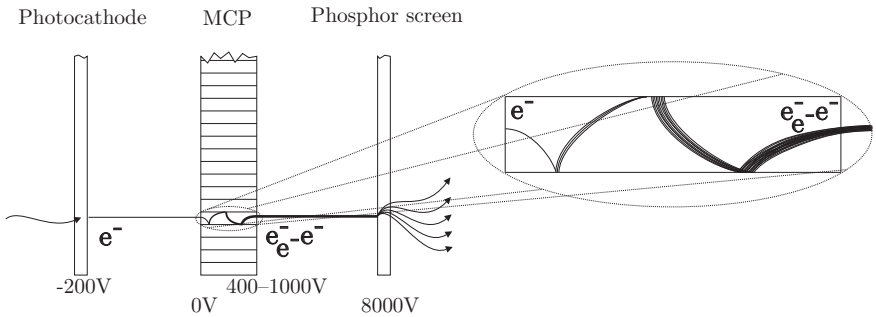

Figure 2.1: *Schematic of a one-stage image intensifier. The voltages given in the figure are typical and vary between models.*

electrons, the electrostatic repulsion and the spread of the electron bunch being reduced accordingly. However, this solution is generally limited by the low brightness of the signal in combination with limitations in the sensitivity of the detector. A second disadvantage is the nonlinear response that the charge depletion in the MCP brings about [15, 16]. This phenomenon has been studied in detail and will be described in the section that follows.

2.3.1 MCP charge depletion

In this subsection, a description of the phenomenon of MCP charge depletion is followed by the presentation of a model and of a method for experimentally characterizing the defect.

In the absence of any amplification, the stored charge in the MCP, Q_s, can be described as

$$Q_s = V_s C \tag{2.1}$$

where C is the MCP capacitance, and V_s refers to the voltage applied over the MCP. During the amplification of a signal, electrons are drained from the MCP and the charge is thus decreased. If the amplified signal – in terms of charge drained from the MCP – is comparable to the stored charge, the gain will be lower towards the end of the signal pulse than in the beginning. This effect can, although weakly, be seen in Fig. 2.2, in which the output signal is plotted against the input signal for a given MCP voltage (compare the linear and the quadratic fit of the data). The gain, corresponding to the slope of the curve is lower for the higher signal levels, indicating that charge depletion has occurred. For a single recording, where the MCP is initially in an unaffected stage, as in the case shown in Fig. 2.2, this effect is often small and within tolerable error margins. If not, the nonlinearity can be measured and be fitted with use of a simple function (as in Fig. 2.2), to be used in the correction of later recordings. One example in which this artifact is problematic is that of temperature measurements based on ratios of signals in two different spectral regions, as reported in [16].

After depletion of the MCP charge, it is replenished again by the strip current. The characteristic time, RC, where R is the MCP resistance, for the replenishment of the charge is usually in the order of ms, i.e. much longer than the typical length of

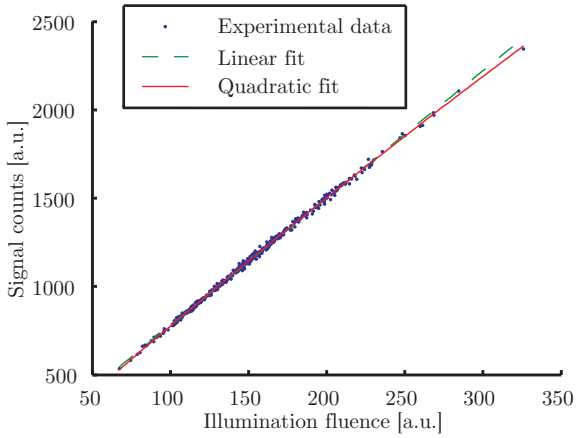

Figure 2.2: *The integrated signal from an image intensifier, shown as a function of the incident fluence (homogeneous illumination). A linear and a quadratic fit are included to guide the eye.*

a signal generated by a pulsed laser source, (~10ns). In such cases the replenishment is insignificant during the amplification process and can be treated as something that only occurs after amplification. However, if the time separation between two consecutive exposures is smaller than RC, the MCP charge will be perturbed already in the initial part of the second pulse. For repetitive exposures at high repetition rates the depletion in the MCP ads up, further supressing the gain in regions of high fluence. Eventually one cannot be sure whether a reduction in the recorded signal level in a region of the image is due to a lower signal from the corresponding position in the measurement volume or to charge depletion in the MCP [15]. In Fig. 2.3, the MCP gain at a repetition rate of 1 kHz and of 20 kHz, respectively, is plotted. In

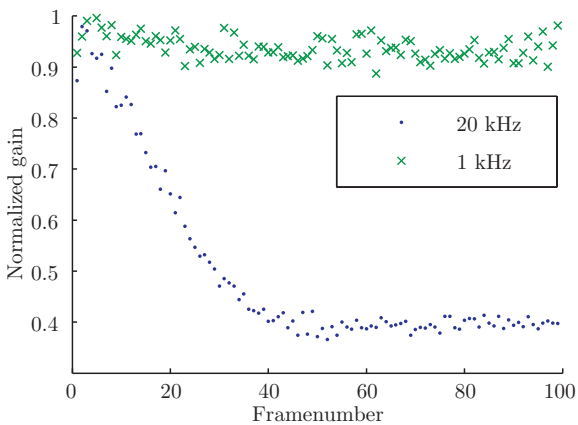

Figure 2.3: *Normalized gain as a function of image number.*

the 1 kHz case the MCP has time to recharge between consecutive exposures. In the

20 kHz case, however, the charge depletion increases until the gain reaches a steady state of about 40 % of the unperturbed value.

Time dependent TLM model.

This subsection contains a short summary of the transmission-line matrix (TLM) based model, as derived for MCP:s by Giudicotti [17], together with a procedure that is outlined of how to fit the model to experimental data.

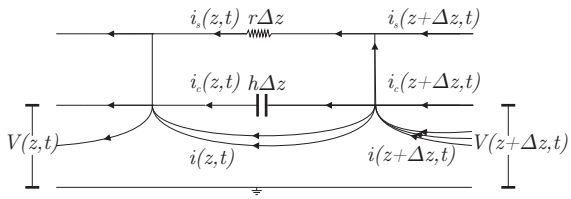

Figure 2.4: *Transmission line model of a continuous channel multiplier.*

From the distributed component electrical network given in Fig. 2.4 the following equations can be derived:

$$\frac{\partial i_s(z,t)}{\partial z} + \frac{\partial i_c(z,t)}{\partial z} + \frac{\partial i(z,t)}{\partial z} \tag{2.2a}$$

$$\frac{1}{r}\frac{\partial V(z,t)}{\partial z} = i_s(z,t) \tag{2.2b}$$

$$\frac{1}{h}\frac{\partial}{\partial t}\left(\frac{\partial V(z,t)}{\partial z}\right) = i_c(z,t) \tag{2.2c}$$

$$\frac{1}{i(z,t)}\frac{\partial i(z,t)}{\partial z} = k\ln\left[\frac{L}{V_m}\frac{\partial V(z,t)}{\partial z}\right] \tag{2.2d}$$

where $V(z,t)$ is the voltage at time t and position z along a MCP tube of length L, and where $i(z,t)$, $i_s(z,t)$ and $i_c(z,t)$ is the signal, the strip and the capacitive current, respectively. The variables $r = {}^{R}\!/_{L}$ and $h = {}^{1}\!/_{CL}$ represents here the resistance and inverse capacitance per unit length, respectively. Equation (2.2d) is called the gain equation for the discrete dynode MCPs, as adapted to continuous multipliers by Giudicotti [17]. Here, k is the gain constant and V_m is the *crossover voltage*, i.e. the voltage applied over the MCP that provides a gain of unity. In the unperturbed case, before any charge has been depleted, the voltage is constant over time and increases linearly along the MCP. In such a case, the solution to Eq. (2.2d) becomes

$$i(z,t) = i_0(t)\mathrm{e}^{Gz} \tag{2.3}$$

where $G = k\ln\left({}^{V_s}\!/_{V_m}\right)$ is the logarithmic gain and $i_0(t) = i(0,t)$ is the incoming signal current, which is proportional to the incident signal.

In case the output current from the MCP is sufficiently large to affect the stored charge, the strip current and strip voltage will no longer be nicely constant and linear, respectively, and Eq. (2.3) is no longer valid. However, the deviation from the ideal

case can be treated as a perturbation.

$$i_s(z,t) = I_s + I(z,t) \tag{2.4a}$$

$$V(z,t) = \frac{V_s}{L} z + \phi(z,t) \tag{2.4b}$$

where $I(z,t)$ and $\phi(z,t)$ are the resistive current and voltage, respectively, in excess of the nominal unperturbed strip current and voltage.

To enable the perturbed signal amplification to be compensated for, a function that describes the initial signal, i_0, on the basis of the final signal, $i_L(t) \equiv i(L,t)$, is required. Thus, we define $g^{-1}(z,t) \equiv {}^{i(z,t)}/_{i_L(t)}$ as being the inverse gain. Based on Eqs. (2.2) and (2.4), $g^{-1}(z,t)$ can be expressed (see appendix A for the full derivation) as

$$\begin{aligned} g^{-1}(z,t) = \exp\Bigg[& G(z-L) + k\int_z^L \ln\Bigg(1 + \frac{L}{V_s}\frac{\partial\phi(z',0)}{\partial z'} + \dots \\ & \frac{h}{L}\int_0^L\int_0^t g^{-1}(z,t')i_L(t')dt'dz - h\int_0^t g^{-1}(z',t')i_L(t')dt'\Bigg)dz'\Bigg] \end{aligned} \tag{2.5}$$

In Eq. (2.5), $g^{-1}(z,t)$ is present on both sides of the equal sign. However, on the right side it is part of the integral that describes the perturbation from the state of an ideal unperturbed inverse gain. Hence, Eq. (2.5) can be solved numerically for $g^{-1}(z,t)$ by iterative execution of

$$\begin{aligned} g_n^{-1}(z,t) = \exp\Bigg[& G(z-L) + k\int_z^L \ln\Bigg(1 + \frac{L}{V_s}\frac{\partial\phi(z',0)}{\partial z'} + \dots \\ & \frac{h}{L}\int_0^L\int_0^t g_{n-1}^{-1}(z,t')i_L(t')dt'dz - h\int_0^t g_{n-1}^{-1}(z',t')i_L(t')dt'\Bigg)dz'\Bigg] \end{aligned} \tag{2.6}$$

until it converges. In the first iteration, $g_0^{-1}(z,t) = \mathrm{e}^{G(z-L)}$ is set as an approximation of the inverse gain.

Prior to the initial exposure, the excess electric field, ${}^{\partial\phi(z,0)}/_{\partial z}$, is zero. However, if the MCP is exposed again before it has had time to recover, the excess electric field is non-zero and can be expressed as

$$\frac{\partial\phi(z,t)}{\partial z} = \frac{\partial\phi(z,\tau)}{\partial z}\mathrm{e}^{-t/RC} \tag{2.7}$$

Here ${}^{\partial\phi(z,\tau)}/_{\partial z}$ is the excess electric field at the end of the previous exposure. It can be expressed as

$$\frac{\partial\phi(z,\tau)}{\partial z} = \frac{\partial\phi(z,0)}{\partial z} + \frac{h}{L}\int_0^L\int_0^\tau g^{-1}(z,t')i_L(t')dt'dz\ldots - h\int_0^\tau g^{-1}(z,t')i_L(t')dt' \tag{2.8}$$

Experimental implementation

In practice, the MCP-specific quantities V_m, h and k, in Eq. (2.6), and RC in Eq. (2.7) can be treated as unknowns. To determine these, the problem can be divided into three parts: the *unperturbed gain*, the *perturbed gain* and the *gain recovery*. To examine the *unperturbed gain*, the image intensifier is exposed to a continuous light source sufficiently low in irradiance as to not perturb the MCP electric field. If both $i(z,t)$ and $i_0(t)$ are measured for different voltage gain V_s, then Eq. (2.3) can be fitted to the dataset in order to extract the parameters k and V_m. However, neither $i(z,t)$ nor $i_0(t)$ is easily accessible. Instead, two high-speed cameras are set up as shown in Fig. 2.5 in order to record the relative irradiance before and after the image intensifier. The data recorded by the cameras can be expressed as

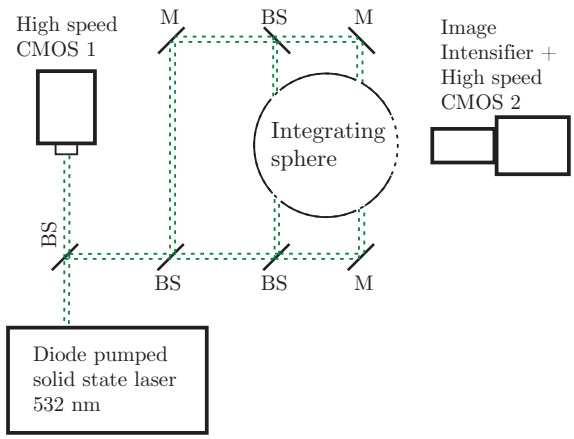

Figure 2.5: *Schematic figure of the experimental setup for MCP characterization.*

$$S_1 = c_1 \int_0^T i_0(t)dt = c_1 Q_0 \tag{2.9a}$$

$$S_2 = c_2 \int_0^T i_L(t)dt = c_2 Q_L \tag{2.9b}$$

where T is the exposure time of the intensifier and the cameras, and Q_0 and Q_L are the charge at the end of the exposure, i.e. the integrated signal current in the beginning and in the end of the MCP, respectively. The constant, c_1, includes the collection efficiency of camera 1, the ratio of the irradiance at camera 1 to the irradiance at the image intensifier, and the inverse collection efficiency of the photocathode in the image intensifier. The constant, c_2, includes the gain in the phosphor screen and (if present) the booster stage of the image intensifier, the transitivity and the magnification in the relay optics between the image intensifier and camera 2, and the collection efficiency of camera 2. By integrating Eq. (2.3) over T and setting $z = L$, one can express the ratios of the individual signals to one another as

$$\frac{S_2}{S_1} = \frac{c_2}{c_1}\frac{Q_L}{Q_0} = \frac{c_2}{c_1} \mathrm{e}^{\ln\left(\frac{V_s}{V_m}\right)kL} \tag{2.10}$$

In Fig. 2.6 the unperturbed gain, i.e. the ratio of the initial to the final signal charge, is plotted as a function of the voltage V_s, that is applied across the MCP. Equation 2.3 is fitted to the data with V_m, k and c_2/c_1 being unknown variables. A

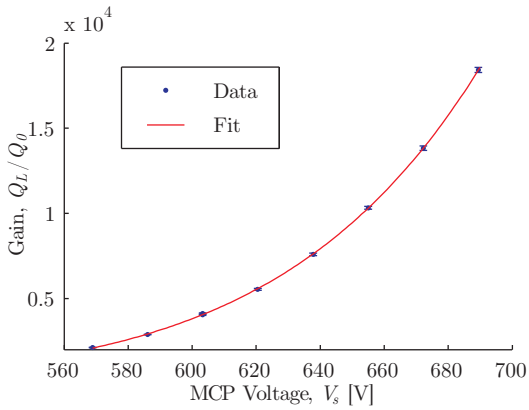

Figure 2.6: *The gain, i.e. ratio of the two charges Q_L and Q_0 as a function of the Voltage applied over the MCP. The fit of Eq.* (2.3) *is shown as a solid line.*

value of the *crossover* voltage $V_m = 290$ V can be extracted from the fit, and be attributed to the particular image intensifier investigated here.

To examine the *saturated gain*, the unperturbed intensifier is exposed to a short pulse ($\tau << RC$), during which the charge regeneration via the strip current is negligible. Under these conditions, Eq. (2.6) is valid and can, with the expression of the recorded signals as given in Eq. (2.9), be written as

$$g_n^{-1}(z,t) = \exp\left[G(z-L) + k\int_z^L \ln\left(1 + \frac{L}{V_s}\frac{\partial\phi(z',0)}{\partial z'} + \dots \right.\right.$$
$$\left.\left.\frac{S_2}{L}\frac{h}{c_2}\int_0^L\int_0^t g_{n-1}^{-1}(z,t')dt'dz - S_2\frac{h}{c_2}\int_0^t g_{n-1}^{-1}(z',t')dt'\right)dz'\right] \tag{2.11}$$

Here, h/c_2 is unknown. To find h/c_2 one compares Eq. (2.11) with the measured data.

$$\int_0^\tau g^{-1}(0,t)dt = \int_0^\tau \frac{i(0,t)}{i(L,t)}dt = \frac{S_1}{S_2}\frac{c_2}{c_1} \tag{2.12}$$

Thus, during each iteration of Eq. (2.11), it is fitted to the sampled data, with h/c_2 serving as the unknown, by minimizing the error in

$$\int_0^\tau g_n^{-1}(0,t)dt - \frac{S_1}{S_2}\frac{c_2}{c_1} = 0 \tag{2.13}$$

with c_2/c_1 being as found by measurement of the *unperturbed gain*.

To uncover the gain recovery, multiple consecutive short exposures ($\tau << RC$) are recorded at varying time separation ($T < RC$). The excessive electric field at the

end of each pulse is calculated using Eq. (2.8) combined with Eq. (2.9) as

$$\frac{\partial\phi(z,\tau)}{\partial z} = \frac{\partial\phi(z,0)}{\partial z} + \frac{S_2}{c_2}\frac{h}{L}\int_0^L\int_0^\tau g^{-1}(z,t')dt'dz - \frac{S_2}{c_2}h\int_0^\tau g^{-1}(z,t')dt' \quad (2.14)$$

If RC had been known, Eq. (2.7) could have been used to calculate the recovery of the electric field, but since RC is unknown, Eq. (2.7) is combined with Eq. (2.11) for an estimation of the inverse gain in the next exposure.

$$\begin{aligned} g_n^{-1}(z,t) = \exp\Bigg[& G(z-L) + k\int_z^L \ln\Bigg(1 + \frac{L}{V_s}\frac{\partial\phi(z',\tau)}{\partial z'}\mathrm{e}^{-t/RC} + \dots \\ & \frac{S_2}{L}\frac{h}{c_2}\int_0^L\int_0^t g_{n-1}^{-1}(z,t')dt'dz - S_2\frac{h}{c_2}\int_0^t g_{n-1}^{-1}(z',t')dt'\Bigg)dz'\Bigg] \end{aligned} \quad (2.15)$$

The value obtained from Eq. (2.15) is compared with the measured value of the inverse gain at this exposure according to Eq. (2.13), but with RC set as the free parameter during minimization of the error.

When all the unknowns, RC, h/c_2, k and V_m, have been found, it is possible to compensate for the effects of charge depletion in the post-processing of data recorded by the same image intensifier. Eqs. (2.15) and (2.14) are then sufficient to calculate the unperturbed initial signal, without the need of monitoring the incident irradiance by use of camera 1. However, if the detector attached to the intensifier is different than that used during characterization, any change in collection efficiency and resolution has to be compensated for in c_2.

Chapter 3

Time Resolved 3D Imaging

ALTHOUGH 2D investigations based on laser-sheet illumination may provide precise data in the targeted cross-section, there is a risk for misinterpretation of the data due to the missing out-of-plane information. Out-of-plane bridging of the flame front may be interpreted, for instance, as a detached flame. Also, quantities such as flame curvature, strain and displacement speed would be incorrectly calculated if based on a 2D image. Although it has been shown that the error in these variables can be compensated for by multiplying by a factor, such as $\pi/4$ for displacement speed [18], this is valid only on average and for isotropic flames. If the information is required not only on a statistical basis alone, the measurement needs to be extended to the third spatial dimension.

A common approach to determining the flow field is to seed particles into the flow and measure their trajectories. This approach can be extended to three dimensions by employing a holographic [19], stereoscopic [20], tomographic [21]or laser sheet scanning (LSS) method [22]. For optical diagnostics techniques in which the contrast in the signal is not as great as in images of particles seeded to the flow, techniques that rely on the identification of features in different images is less feasible [23]. To record such signals, technical solutions based on LSS appear to be the better option. It was demonstrated already in 1987 that a high repetition rate laser combined with LSS and a framing camera provides the means for 3D imaging of various species and turbulent flows [24, 8]. When the signal yield is high, a long laser pulse extended over the entire scan can also be used [25]. For higher fluence and almost instantaneous recording, a cluster of high power Nd:YAG lasers is an option that has been pursued in the measurement of fuel distribution [26], and soot volume fraction through use of laser-induced incandescence (LII) [27]. The recent development of high power pulsed burst lasers has enabled LSS based 3D imaging of turbid flows at high spatial depth resolution to be carried out. All of the aforementioned techniques have the capability of recording single shot 3D data, but do not provide with any temporal information. The high repetition rate of the DPSS Nd:YAG and dye laser system together with CMOS cameras and a high repetition rate image intensifier makes it possible to follow transient behavior in 2D cross-sections of turbulent flows. However, if some of the time resolution is sacrificed, it is possible to extend the recording to also cover the third spatial dimension, as is shown in Papers I and II. The present chapter

is concerned with the experimental methodology developed in the work reported in these papers. First, considerations regarding the experimental setup are discussed, with special emphasis being placed on the method being employed to achieve a linear scan. Thereafter, different experimental applications together with associated data evaluation methods are presented.

3.1 Experimental setup and considerations

The optical setup required for 3D imaging based on LSS is in many respects similar to the one used for planar laser illumination. The main differences lie in the scanning of the laser sheet and the increased depth of field required for the detector to be able to record sharp images throughout the measurement volume.

A common approach to forming a laser sheet for planar laser illumination is to combine a negative cylindrical lens with a positive spherical lens and align them with overlapping focal points. In such a setup, the laser beam is expanded and re-collimated with the desired sheet height in the one dimension (see Fig. 3.1 **b**) and is focused at the measurement volume in the other (see Fig. 3.1 **a**). The same basic setup

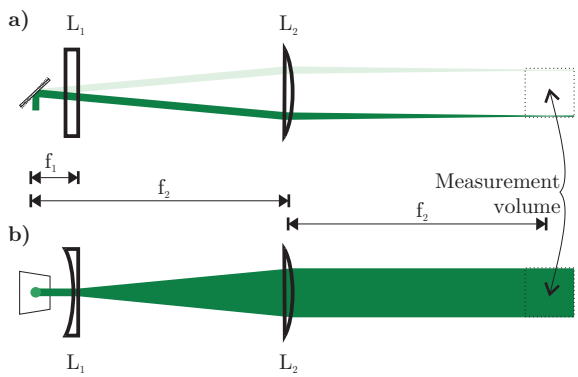

Figure 3.1: ***a*** *top view and* ***b*** *side view of a typical sheet-forming setup for laser-sheet scanning applications.*

can also be used to create a scanning laser sheet. To achieve a parallel displacement of the laser sheet during the scan, the scanning mirror is placed at the common focal point of the lenses, as shown in Fig. 3.1.

3.1.1 Scanning of laser sheet

For the deflection of the laser beam required to achieve the displacement of the laser sheet that is desired, different practical solutions are available. The most straightforward approach is probably to use a galvanometric-driven mirror as was done in [28]. Although such a solution is straightforward and practical – one simply feeds the galvanometer with the desired deflection pattern – the response time limits the scan frequency to ~1 kHz. When the galvanometer is driven to its maximum displacement speed, the inertia of the system causes the deflection to deviate from the deflection pattern that is given. Thus, for higher scan frequencies a resonant scanner

is probably a better choice. Here the mirror is mounted on a torsion bar instead of on bearings. The stiffness of the bar together with the mirror mass are balanced so as to obtain an eigenfrequency in the oscillation of the mirror corresponding to the desired scan frequency. A resonant scanner produces a sinusoidal deflection pattern, oscillation frequencies of up to ~10 kHz being currently available on the market. For higher frequencies, the mirror has to be very small, it is then becoming difficult to achieve lossless reflection of the laser beam without burning of the mirror surface. For scan frequencies in the 100 kHz range, rotating polygons provide a more suitable approach [29]. However, in the thesis emphasis is placed on a scanning system based on use of resonant scanners.

Linear scan from resonant scanners

A major problem in the use of resonant scanners as a means of deflection of the laser sheet is the sinusoidal nature of the resonant oscillation. If the laser is operated at a constant repetition rate, which is recommended for stability of the output, the laser sheets are more closely spaced in the outer part of the oscillation than in the center of each scan. In the design of an experiment, the scanning amplitude is decided based on a compromise between attainment of a large recording volume and of a high spatial resolution. If the laser sheets are unevenly spaced, a particular requirement on the spatial resolution results in the measurement volume being reduced. Thus, the scan should ideally be linear, i.e. show a scan pattern in the form of a triangular instead of a sinusoidal wave. A triangular wave, $f(t)$, can be expressed in a Fourier series as

$$f(t) = \lim_{k\to\infty} f_k(t) = \lim_{k\to\infty} \frac{8}{\pi^2} \sum_{n=0}^{k} (-1)^n \frac{\sin\left((2n+1)\,\omega t\right)}{(2n+1)^2} \tag{3.1}$$

where ω is the angular frequency. Thus, a sine wave can be transformed into a triangular wave by adding the odd overtones of the sinusoidal with decreasing amplitude and alternating phase, as shown in Fig. 3.2. In an optical arrangement, the deflection from the base frequency and its overtones can be added together using multiple oscillators, at the corresponding frequencies, in 4f-setups according to Fig. 3.3. Since the number of overtones that can be added together according to Fig. 3.3 is limited by practical constrains, it is not possible to obtain a perfect triangular deflection, as would be the case with Eq. (3.1) fulfilled. Thus, one have to settle for an approximation. Fortunately, the amplitude of the overtones in Eq. (3.1) decreases with the square of the order and $f_k(t)$ converges rapidly as k increases. Thus, a deflection similar to a triangular wave can be achieved with a limited amount of overtones in the summation. Such a deflection can be further linearized by optimizing the individual amplitudes of the respective mirror oscillations for a given k. In Fig. 3.4, the deflections from two mirrors, one operating at the base frequency and the other at the first odd overtone, have been added together, both experimentally and in a numerical simulation. The coefficient of determination, R^2, in the fit of a linear curve to the laser sheet positions during a single sweep is plotted as a function of the relative amplitudes in the oscillations of the mirrors. The repetition rate of the laser was adjusted here to provide ten laser pulses during each scan. As seen in the results of the numerical simulation as given in Fig. 3.4, the optimal amplitude of the first odd overtone (marked by an x) is slightly lower than what could be anticipated from

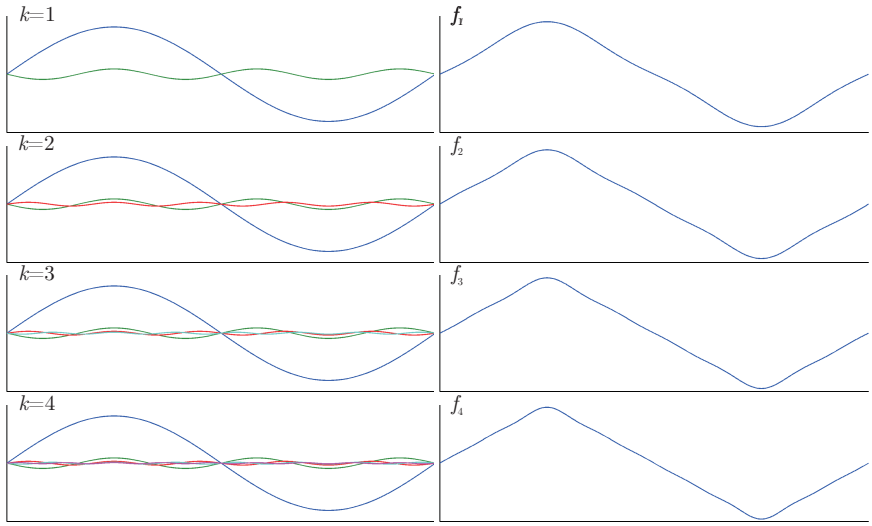

Figure 3.2: *Calculation of $f_k(t)$ in Eq.* (3.1) *for different values of k. The individual sine waves are plotted to the left and their sum to the right.*

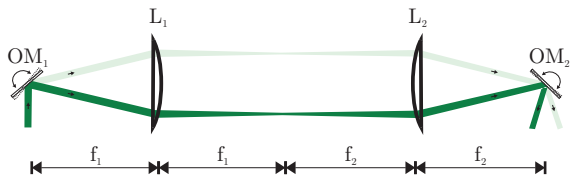

Figure 3.3: *Schematic of a 4f-setup where the deflection from two mirrors are added together. Oscillating Mirror (*OM*), Lens (*L*), focal length (*f*).*

Eq. (3.1) (marked by a dashed line). The experimental values are slightly offset in the direction of lower amplitudes. The reason to this is probably that the monitor signals used to estimate the oscillation amplitudes are not completely linear. Noticeable is also the fact that the accuracy of the fit to the experimental data appears to exceed what is theoretically possible (since the maximum of the numerical data is lower than the maximum of the experimental data). A possible explanation of this phenomena is that the oscillation of the mirrors are slightly driven and is thus not fully harmonic.

Laser sheet position

The positions of the laser sheets in the measurement volume are determined by the timing of the laser pulses in relation to the phasing of the mirror oscillators. Since the driver of the mirror oscillators – employed in the work reported in the thesis – lack any option for external synchronization, the main oscillator is set as the master clock for the measurement system. The oscillator driver provides a monitor signal proportional to the mirror deflection. This signal is used – once per period – to trigger a pulse generator to produce a burst of pulses for the triggering of the laser, the detectors and the image intensifier. The number of pulses in the pulse burst is

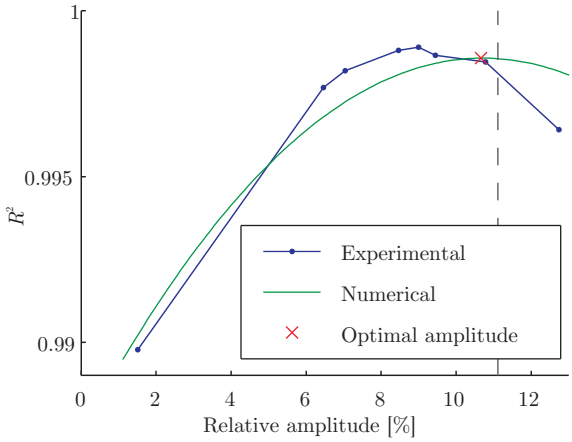

Figure 3.4: *Coefficient of determination, R^2, of a linear fit to the laser sheet positions shown as a function of the relative amplitude in the oscillation of the first odd overtone mirror. Both experimental and numerical data are given. The maximum in the numerical simulation is marked by a cross, and the maximum anticipated from Eq.* (3.1) *is marked by a dashed line.*

equal to the number of laser sheets desired during each period, the frequency being equal to that of the main oscillator times the number of pulses. In this way, the laser sheets end up at the same position in each period of the mirror oscillation, with an equal time separation between pulses.

Although the frequency of the oscillators is fixed to the predetermined eigenfrequency, it is still possible to control somewhat the temporal resolution of the recorded 3D data by adjusting the phasing between the laser pulses and the mirror oscillation. In Fig. 3.5 examples of the measured sheet position for two different settings of the phase are presented. In Fig. 3.5 **a** the timing is set so that the laser sheets end up

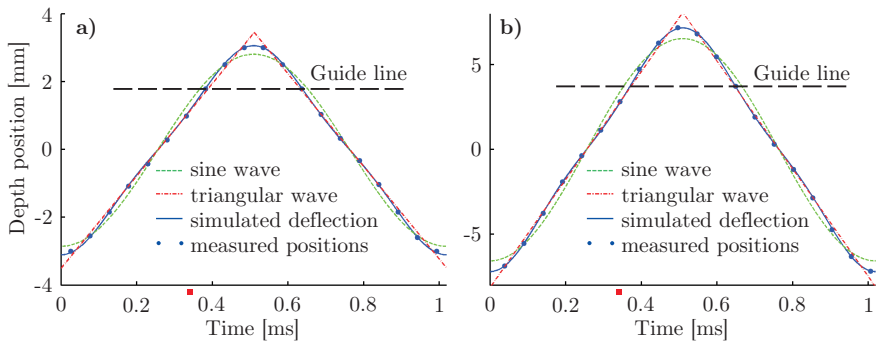

Figure 3.5: *Measured sheet positions for* **a** *overlapping laser sheet positions and* **b** *separated sheet positions in the two scan directions. A guideline is inserted to emphasize the difference. The scanner is operated at* 970 Hz *and the laser is operated at* 19.4 kHz *(20 laser pulses per period).*

at the same position regardless of sweep direction. Thus two 3D images are recorded

during each period in the mirror oscillation. In Fig. 3.5 **b** the timing is instead shifted to achieve an even spread of the laser sheet positions during the period as a whole. The former approach is pursued when the temporal resolution is more important than the spatial one, as in Paper II, and the latter approach is pursued whenever the requirement of temporal resolution is low in relation to the oscillation frequency, as in Paper I. In Fig. 3.5 the laser sheet positions have been measured by inserting a thin diffuser into the measurement volume and imaging it by use of a high speed camera. The precision in the laser sheet positions can be calculated on the basis of the measured positions. The precision is limited mainly by the time jitter induced in the triggering of the pulse generator by the sinusoidal output of the mirror oscillator driver. In the setup reported in Paper II, the standard deviation of the sheet positions is 12 µm. This is less than the laser sheet thickness, which generally is greater than 100 µm, and is thus not the limiting factor for the depth resolution. However, if the precision needs to be improved, this can be done by changing the triggering to a CW laser reflected onto a photo diode via the oscillating mirror, as is done in [27].

3.1.2 Detection considerations

Detection of the planar laser-induced signal is normally achieved by use of a detection lens and of a detector oriented perpendicular to the laser sheet. In experiments with limited signal yield, such as planar laser-induced fluorescence (PLIF), the signal is generally maximized by use of a collection lens that enables a large collection angle, i.e. low f/#, to be employed. In the imaging of signals induced by a scanning laser sheet, however, the increased requirement in depth of field there limits to the maximum collection angle that can be employed. The depth of field can, as a first approximation, be expressed as

$$DOF \cong 2Nc\frac{m+1}{m^2} \tag{3.2}$$

where c is the circle of confusion, N is the f/# and m is the magnification. If an image intensifier is used for collection of the signal, this is usually what limits the resolution in the focal plane. Equation (3.2) can be employed for calculating which f/# provides the same resolution throughout the measurement region as a whole. However, if the f/# needs to be increased, less light is collected and the image intensifier may have to be operated at a higher gain level. This reduces the resolution and may also impose requirements on the post processing, such as spatial filtering, which reduces it even more. Thus, the optimal resolution could be achieved with a lower f/# than initially indicated by Eq. (3.2).

For proper interpretation of the laser-induced signal, it is often essential to know the fluence in each pulse, i.e. the pulse energy and spatial energy profile. With use of stable lasers, this is most easily achieved by making a separated recording before and/or after the main measurement, with the assumption that the fluence stays constant throughout the measurement period. DPSS lasers can be stable if operated at their intended operating point. However, when pushing the pulse frequency to the maximum of what the laser can deliver, the output decreases towards the lasing threshold and becomes unstable. As was shown in Paper II it is not only the pulse energy that fluctuates, but also the spatial energy profile. It is thus not sufficient

to measure the pulse energy on a pulse to pulse basis. The energy profile can be recorded by reflecting a fraction of the laser sheet energy into a dye cuvette. The fluorescence from the dye can then be recorded by the same camera as that which records the main signal, as in Paper I, or by a separate camera, as shown in Fig. 3.6 (a sheet profiler). If the dye is excited in the linear regime, the fluorescence obtained is proportional to the laser sheet energy profile. One matter that should be considered

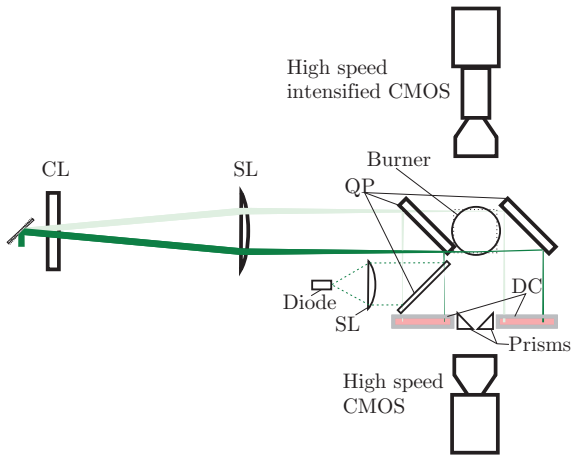

Figure 3.6: *Schematic of a setup for pulse to pulse detection of the spatial energy profile: Cylindrical Lens (CL), Spherical Lens (SL), Quartz Plate (QP) and Dye Cuvette DC.*

is the vignetting effect, that is caused by the walls in the dye cuvette. Part of the light emitted towards the camera lens is blocked by the cuvette wall. This effect is more significant for the light origin furthest away from the camera. Thus, the recorded energy profiles cannot be compared directly with each other before the sheet profiler sensitivity at different sheet positions has been calibrated against a second detector (the diode in Fig. 3.6).

3.2 Experimental applications and data evaluation

One advantage that comes with the use of LSS as means of acquiring 3D data is the portfolio of already developed and well established measurement techniques based on laser sheet illumination that are available. Basically any diagnostic technique that rely on planar laser illumination can be extended to the third spatial dimension and time through use of LSS. The only limitations are those in terms of repetition rate and pulse energy that are set by the hardware of the measurement system. The repetition rate must be faster than the dynamics of the flow, which limits the investigations that are possible to flows of moderate flow rate. The pulse energy needs to be sufficient high to provide an adequate S/N. With the limited pulse energy that DPSS lasers provide as compared with 10 Hz systems, the investigations have been restricted thus far to use of techniques with a high signal yield. Included in the thesis, are a demonstration of the experimental method by the recording of light scattered on water droplets (MIE scattering) in Paper I, and its application in Paper II to a flame in a study in which LIF from the OH radical is recorded and analyzed.

3.2.1 Flame front detection

Tracking of the flame front under turbulent combustion conditions is important both for model validation and for investigation of the flame-flow interaction in flame stabilization processes [30, 31]. A common definition of the flame front is the region of maximum heat release in the reaction zone [32]. In earlier research aimed at determining the flame fronts position, measurements have been made of a varity of intermediate combustion species, such as CH [33], CH_2O [34], OH [30, 35] or a combination of CH_2O and OH [36]. OH is the species most commonly targeted for flame front determination purposes, the position of the flame front being estimated there on the basis of the maximum levels for the gradients of recorded OH PLIF signals. Although that technique is inferior to a variety of other techniques in terms of accuracy, it is used frequently because of the high signal yield that is obtained, which provides superior S/N. Such an approach is a particularly attractive option for applications in which the laser fluence that is available is low, such as in the case of high repetition rate PLIF [7].

Edge detection

Before an accurate representation of a flame front can be extracted from OH signals the high frequency noise introduced by the image intensifier needs to be suppressed. This is commonly achieved by employing a Gaussian low pass filter. For noisy data, a nonlinear diffusion filter can be used to further suppress the noise while preserving the continuous gradients in the data [37].

The flame fronts can be extracted from the filtered image by calculating and thresholding the gradients in the data. However, for increasing the robustness of the results obtained and reducing the sensitivity of the gradient to noise, a slightly more sophisticated detection scheme, named the Canny edge detection, has become the established approach [38, 32]. In the Canny edge detection scheme the gradient is calculated and two thresholds based on the maximum gradient intensity are defined. Values exceeding the high threshold are interpreted as stemming from parts of the edge (in this case the flame front), whereas regions in which the low threshold is exceeded are only considered to be part of the edge if they neighbor on some other region in which the high threshold is exceeded. In this way parts of the apparent flame front that are stretched out or for some other reason show a lower gradient, may still be interpreted as being part of the flame front without the noise associated with similar gradient values being included. One disadvantage of the original Canny edge detection scheme is that the thresholds obtained are based on the maximum gradient intensity found for each image. Thus, in the evaluating a series of images the definition of what is to be interpreted as a flame front varies, making the data evaluation uncertain. This is especially troubling in scanning laser sheet applications, since some of the images may be recorded solely in the burnt region, without the flame front being intersected. In such images, the maximum gradient obtained is low, since it originated in fluctuations in the OH distribution within the burnt region, considerable noise thus being interpreted as belonging to a non-existing flame front. Thus, a better approach is to compensate the signal for fluctuation in the laser fluence and define constant values for the thresholds for all recorded images.

Post filtering

For each individual image, it is generally possible to find filtering and threshold parameters that provide a correct representation of the flame front without the inclusion of "false edges". However, it is more challenging to find a common set of parameters that manage this through use of large data sets containing thousands of images. In data with low S/N this is difficult and may even be impossible. In Paper II this problem is solved by setting the threshold values in the Canny edge detection algorithm low, thus including noise in the detected edges, and then employing an additional filter for the removal of the falsely detected edges. This filter is, as all filters are, based on a prior knowledge of the properties in the signal and in the noise. Use of the filter that is employed can be summarized by a series of selection rules, differentiating the flame fronts from false edges. The filter described below is one created for a premixed Bunsen burner flame as is investigated in Paper II. It can thus not be generalized to simply any flame (although it can be modified to suit other flames). The filter accepts the detected edges as being part of the flame front if the following criteria are fulfilled:

- In the direction from the unburnt region towards the burnt region the gradient must be positive. If an edge is detected in fluctuations in the burnt gas region, the situation is usually the opposite.
- The edge must either...
  - start and end at the position of the burner nozzle, as the main flame does.
  - form a closed circle, as if detached from the main flame or bridging in from out of plane.
  - be attached on both sides to the top of the image (the same as above but traveling out of the image).
  - be one of a pair of edges that is attached on the one side to the burner and on the other side to the top of the image, as if it were part of a flame that extends to outside the imaged area.
- The unburnt region must partly overlap the unburnt region in a neighboring plane.

If the above filtering requirements are not sufficient the next step is to infer knowledge of the temporal behavior of the flame. One has to be careful though not to filter away any unexpected but real data.

Data interpolation

An important consideration in 3D imaging based on the scanning of a laser sheet is the time it takes to record a single 3D image. To make correct 3D reconstructions, the data from a given scan has to be recorded within a time period during which the flow and chemical reaction have not altered the distribution of the scalars that are recorded. However, even with use of pulse burst systems, operating at 100 kHz [39], a strict obedience to this requirement would limit the investigations that are possible to laminar flows. A better approach then is to accept the fact that the images

are recorded at different positions in time, and to treat them as such. In direct comparisons with modeling data, the data from the model can be freely extracted at different time position and from different cross-sections. However, for further analysis of the flame front, one may want to calculate the entire surface at a specific position in time. For time-resolved 3D imaging this is possible by interpolating the spatial position of the flame front in a given scan to a common temporal position. To minimize the longest interpolation time, the target time for the interpolation should be set equal to the central scan position, as indicated in Fig. 3.7. An example of

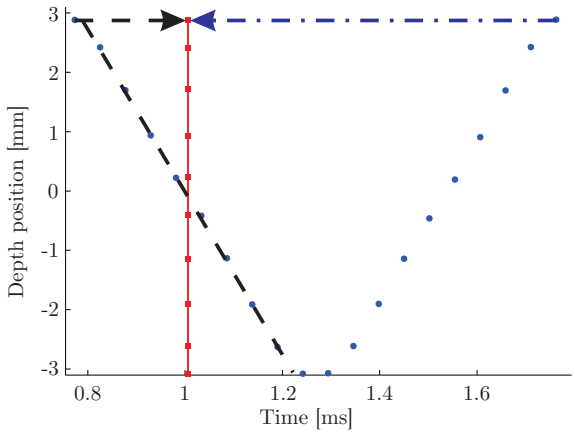

Figure 3.7: *The measured depth positions of the laser sheet during a given period of scanning are represented by circles. The squares and the vertical line indicate the position and the target time for the interpolations. The arrows represents the interpolation process for one of the depth positions.*

the impact of the time interpolation on the evaluated flame fronts is given in Fig 3.8. There the flame front at the center of the flame (corresponding to the position marked by arrows at the top of Fig. 3.7) is plotted at four consecutive time position, both before and after time interpolation. To emphasize the effect, a subset of the data of high displacement speed of the flame front is shown at the position of the sheet having the strongest impact by means of the time interpolation.

An example of the resulting flame front can be seen in Fig. 3.9. There, the surfaces have been fitted to the calculated flame fronts by use of non-uniform rational B-splines (NURBS) [40].

3.2.2 OH concentration

Measurements of the concentration of minor species in combustion can provide valuable data for model validation. Several PLIF-based techniques have been developed during the last decades in the pursuit of reliable quantitative concentration measurements. As a first approximation, the fluorescence that is emitted can be treated as being proportional to the concentration of the targeted species. If the proportionality constant is known, the concentration of the species can be calculated from the fluorescence signal. However, as the excited molecules collide with neighboring molecules the energy may be transferred and be transformed to heat, effectively

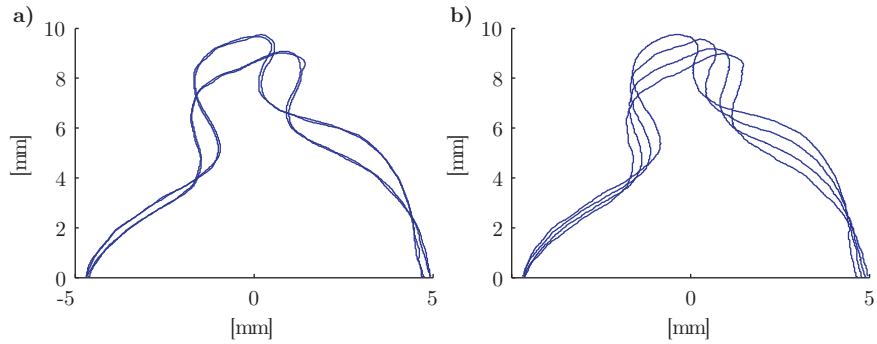

Figure 3.8: *The flame fronts in the center of the flame, corresponding to one of the endpoints in the scan. In* ***a*** *the flame fronts are plotted prior to time interpolation, whereas in* ***b*** *the flame fronts have been interpolated to the central time positions.*

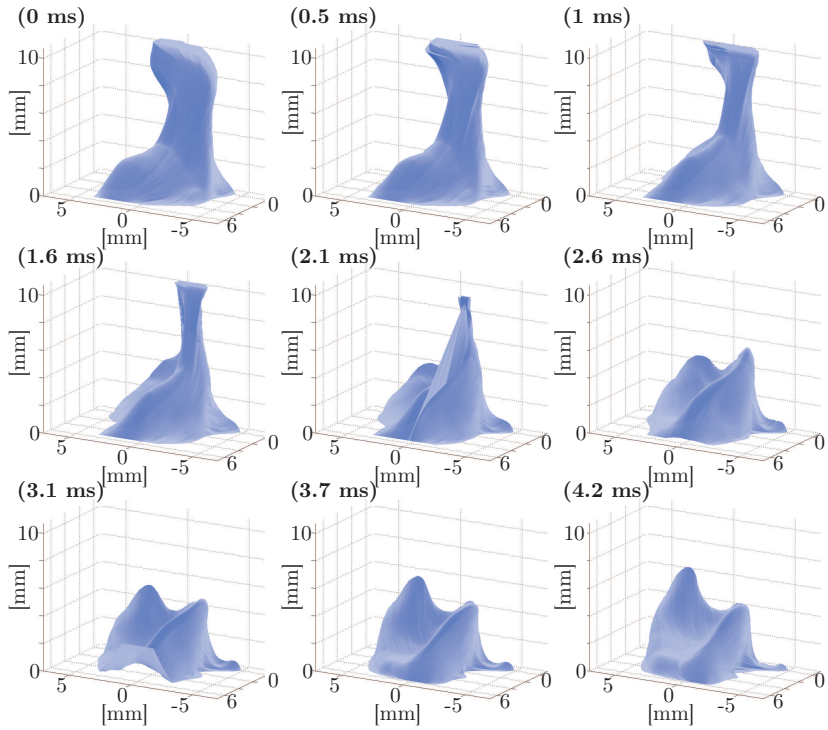

Figure 3.9: *Nine out of 1000 3D images of the calculated flame fronts recorded at 2 kHz. After low-pass filtering, nonlinear diffusion filtering, Canny edge detection, post filtering and time interpolation have been carried out, the 2D flame fronts that have been identified were connected by use of NURBS interpolation.*

quenching the radiation that would otherwise have been emitted. The rate of collisional quenching depends on such factors as species composition, temperature and pressure. Thus, if these factors vary within the flame, the fluorescence is no longer proportional to the concentration of the targeted species. For fully quantitative measurements, collisional quenching thus needs to be taken into consideration.

One approach that may be implemented to overcome the quenching problem is referred to as *saturated PLIF* [41]. With a sufficiently high fluence, the population of the excited state approaches the population in the ground state. At this limit, the quenching becomes irrelevant and can be neglected. The main problem in connection with this technique is that it requires that the laser sheet is in the shape of a top hat, both spatially, temporally and in the frequency domain. Even if this could be achieved, the high pulse energy required to reach saturation makes it difficult to apply the technique in high-repetition-rate systems.

Another option for overcoming the quenching is to excite the molecule to a predissociative state [42, 43]. If the dissociation rate becomes much higher than the quenching rate, quenching becomes insignificant and can be neglected. However, due to the predissociative nature of the excited state, the fluorescence quantum yield is significantly lower than for a stable state. Thus, the approach is not suitable for LSS-based time-resolved 3D imaging in which the laser fluence and detection capabilities are limited.

In a third approach, the quenching rate is calculated from the measured lifetime of the fluorescence signal [44]. Recently, it was shown that this approach can be extended to 2D measurements, referred to then as *lifetime imaging* [45]. However, *lifetime imaging* is noise-sensitive and has thus far only been demonstrated to function with use of pico-second laser pulses.

The quenching rate can also be calculated if the temperature and the concentration of the major quenchers are measured using Raman scattering [46]. However, due to the limited signal strength involved, such measurements are limited to 1D.

If measurements are based on absorption instead of emission, the quenching rate becomes insignificant (since the quenching only affects the excited state). Absorption measurements tend to be line-of-sight techniques, in which the measured absorption is integrated though the flame from the light source to the detector. However, by illuminating the flame with two counter-propagating laser sheets, the local absorption can be derived from the subsequent recordings of the LIF [47]. The gradient in the images depends directly on the concentration distribution and indirectly on the attenuation of the laser sheet due to absorption. Since the concentration is the same in the two images and the attenuation is inverted, the absorption, and thus the concentration can be deduced from the ratios of the gradients in the images. Since the technique depends on the ratio of the gradients in two images, it is extremely noise-sensitive and thus requires a high S/N. For high repetition imaging, with limited S/N, this technique is not suitable.

Although the ultimate goal is to obtain fully quantitative measurements resolved in time and in all three spatial dimensions, technical developments are not quite there yet. However, being able to record semi-quantitative time-resolved 3D concentration data where the quenching is not fully quantified but still taken into consideration, may be an important step in that direction. Thus, an approach similar to what is presented in [48, 49], in which the integrated concentration along the laser sheet is used to calibrate the fluorescence along the same path, has been pursued for estimating the

OH number density. In this way the average quenching along the beam path is compensated for.

The local absorption throughout the flame can be calculated by assuming that the total absorption, measured in the basis of the differences in irradiance from the cuvettes in Fig. 3.6, is proportional to the integrated signal recorded in the flame,

$$\sum S_f = Q_f \varepsilon \sum (\Phi_0 - \Phi_f), \tag{3.3}$$

where S_f is the recorded signal, Q_f is the fluorescence quantum yield, ε is the camera function, i.e. the amount of light detected and translated to signal counts in the digitized image, and Φ_0 and Φ_f stand for the initial and the final fluence, respectively. The signal recorded at a given position in the flame can be expressed as

$$S_f = \Phi \alpha' Q_f \varepsilon, \tag{3.4}$$

where $\alpha' = N_n \sigma_0$ is the absorption coefficient, N_n is the number density of the targeted rotational state in the ground state and σ_0 is the effective peak absorption cross-section for the same state excited by laser light having a given spectral profile. By combining Eq. (3.3) with Eq. (3.4) one obtains an expression for the absorption coefficient

$$\alpha' = \frac{S_f}{\Phi} \frac{\sum(\Phi_0 - \Phi_f)}{\sum S_f}. \tag{3.5}$$

As the laser sheet propagates through the flame it is partially absorbed and is thus attenuated. The attenuation of the laser light within the flame can be expressed by use of the Beer-Lambert law,

$$\Phi(x + dx) = \Phi(x) \mathrm{e}^{-\alpha' dx}, \tag{3.6}$$

where dx is the size of a pixel divided by the magnification of the imaging system. For the first excited molecule, i.e. the first pixel column in the recorded image in which the signal is detected, $\Phi = \Phi_0$ and Eq. (3.5) can be used to calculate the absorption coefficient at this location. In the next imaged pixel column, the fluence will have decreased in accordance with Eq. (3.6). Thus, by alternating Eq. (3.5) and Eq. (3.6) the local absorption coefficient can be calculated throughout the flame.

With the effective peak absorption cross-section, σ_0, known, the number density can be calculated from the absorption coefficient $N_n = {}^{\alpha'}/_{\sigma_0}$. The relationship between the effective peak absorption cross-section and the spectrally integrated cross-section can be calculated from the ratio of the peak to the integrated transition in an excitation-scan. Finally, the integrated cross-section can be calculated from the oscillator strength, which in turn can be calculated from numbers that can be found in the literature; see Versluis et al. [47] for details.

Examples of the resulting OH concentration can be seen in Fig. 3.10. Worth mentioning is the fact that, although the data presented in Fig. 3.10 are from the same data set as presented in Paper II, the absolute level of the OH concentration here is approximately four times as high. This is due to an error in the estimation of the relative population in the ground state of the $Q_1(7)$ transition. In Paper II the spin orbital coupling and λ doubling were not taken into account, leading to an overestimation of the relative population by approximately a factor of four.

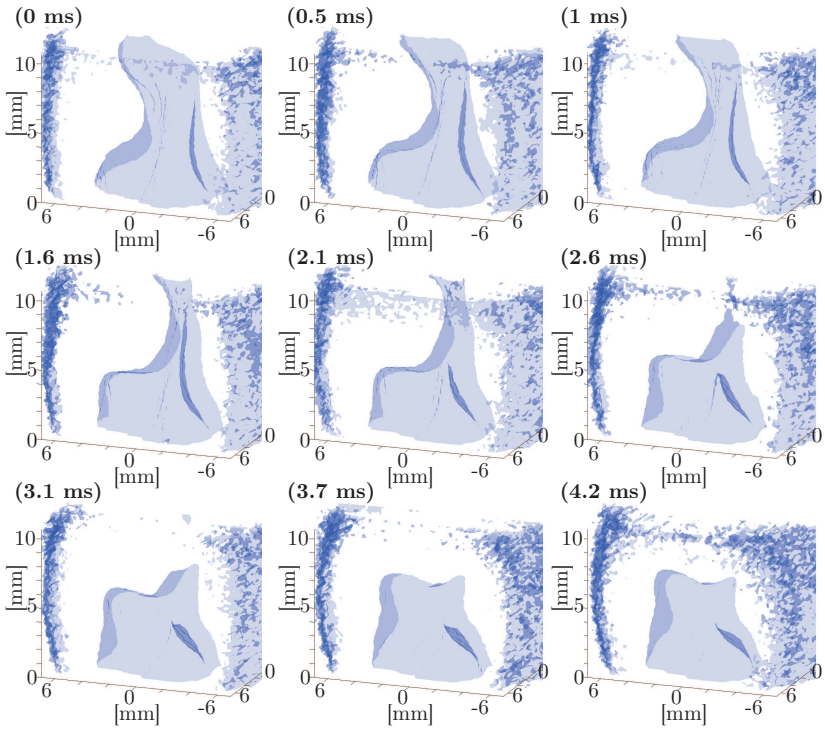

Figure 3.10: *Nine of the 1,000 3D images in a single image sequence. The scanning spans half the flame, the 3D images being recorded at* 2 kHz. *The isosurfaces connect the regions having an OH number density of* $5.5 \times 10^{15}\,\mathrm{cm}^{-3}$, *which corresponds to approximately one-third of the concentration in the flame front. The iso-surfaces are each based on 10 2D OH concentration maps.*

Chapter 4

Quantification of Local Extinction in a Spray

SPRAYS are used in a variety of applications, such as spray painting, medical treatments, soot production, coating and cooling [50]. In combustion applications they are used for fuel injection in internal combustion (IC) engines and gas turbines. The ability to characterize spray properties is of fundamental importance for the development and improvement of spray systems. In the developed part of the spray, where the initial ligaments and filaments have broken up into droplets, the spray can be characterized by the fluid flow and the distribution of droplet size and number density. The most established technique for droplet sizing in sprays, phase Doppler anemometry (PDA), is a point measurement technique, in which the scattered interference pattern from the crossing between two laser beams are analyzed so as to obtain velocity and size information regarding single droplets [51, 52]. Since only one point is measured at a time, the spray has to be scanned, so that only average information can be obtained. To obtain temporal information, or to increase the sampling rate, laser-sheet-based techniques are more appropriate. In one of these techniques [53], the light which is scattered and refracted by droplets that are illuminated by a laser sheet is imaged out of focus on a detector. The distance between the fringes formed by interference between scattered and refracted light carries information regarding particle size. Although it is possible to increase the number of particles that can be detected in a single image by means of optical compression [54], the technique is still limited to relatively dilute particle flows. An optional method that enables measurement to be made in more optically dense environments, in which several particles may reside in the volumes imaged on each pixel of the detector (such as sprays) is often referred to as planar drop sizing (PDS) [55, 56]. It exploits the different properties of the scattering and the absorption cross-sections. For particles substantially larger than the wavelength of the probe light, the scattering cross-section is proportional to the particle area, whereas the absorption cross-section is proportional to the concentration, i.e. to the volume of the particle. Thus the Sauter mean diameter (SMD), which is a parameter commonly used to describe the average particle sizes, can be

calculated as

$$SMD \equiv \frac{\int_0^\infty D^3 dN}{\int_0^\infty D^2 dN} = K \frac{S_f(x,t)}{S_s(x,t)}, \tag{4.1}$$

where D is the particle diameter, $S_f(x,t)$ is the recorded fluorescence signal, $S_s(x,t)$ is the recorded scattering signal, and K is a constant that depend upon the camera functions of the detectors and the concentration and fluorescence quantum yield of the dye.

One of the major challenges for PDS and for optical diagnostics in sprays in general is coupled to multiple scattering (MS) [57]. MS occurs when the light is scattered by more than one particle. MS light that is detected introduces artifacts in the image. It can be argued that the MS light is a minor problem in PDS, if assumed that it cancels out in the ratios of the signals to one another. However, it has been shown that the MS is different in the image of the fluorescence and the elastically scattered light [58]. One approach to quantifying and suppressing the MS light, and thus increasing the accuracy of PDS, is to introduce a spatial modulation to the illuminating laser sheet [59, 60].

The attenuation of the light that propagates through the spray depends both on the absorption and scattering cross-sections and on the number density of the particles. If the absorption in the gas phase can be neglected (which is often the case due to the high degree of absorption and scattering in the droplets), the attenuation can be expressed by the extinction coefficient as

$$\bar{\mu}_e = N(\bar{\sigma}_s + \bar{\sigma}_a) = N \frac{\int_0^\infty n_p(D)(\sigma_s(D) + \sigma_a(D))dD}{\int_0^\infty n_p(D)dD}, \tag{4.2}$$

where N is the number density of the particles, $\sigma_s(D)$ and $\sigma_a(D)$ refer to the scattering and the absorption cross-section, respectively, and $n_p(D)$ is the number of droplets with a diameter of D. If the size distribution is known, the cross-section can be calculated. A measurement of the extinction coefficient would then, based on Eq. (4.2), yield the number density. In this chapter, the experimental challenges caused by the MS and the attenuation in the illuminating laser and signal light are discussed. Solutions to the problems involved are presented, the quantified attenuation being used to calculate the local extinction throughout the spray.

4.1 Laser and signal attenuation

The intensity of the recorded light scattered by droplets within a spray can be expressed as

$$S_s = cIN\bar{\sigma}_s(1-a) \tag{4.3}$$

where c represents the camera function, I the irradiance of the laser light in the scattering volume and a the attenuation of the scattered light between the scattering event and the detector (often referred to as *signal attenuation* or *signal trapping*). According to Eq. (4.3), the recorded signal is proportional to the number density and the scattering cross-section. Unfortunately, the irradiance and the signal attenuation are not constant throughout the measurement volume.

The irradiance at a given position in the measurement volume is given by the initial irradiance I_0, i.e. the irradiance in the laser sheet before it has reached the spray, and the attenuation in the optical path between the light source and the scattering position. It can be expressed by Beer-Lambert law as

$$I(x) = I_0 \exp\left(\int_0^x -\mu_e(x')dx'\right). \tag{4.4}$$

Through use of Eq. (4.4) it is possible to compensate for the attenuation of the laser light. However, for Eq. (4.4) to be valid requires that none of the previously scattered light contributes to the irradiance. Since scattered light only changes direction and does not disappear, it may – if scattered multiple times or if the scattering angle is small – still end up in the measurement volume, as shown in Fig. 4.1.

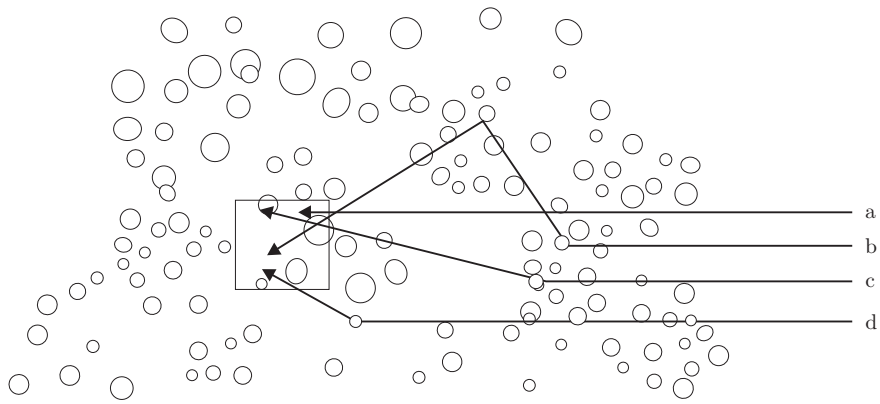

Figure 4.1: *Illustration of MS in a spray. Not only the photons, marked by* ***a****, that are originally directed towards a given position in the measurement volume, can contribute to the irradiation here, but also* ***b****-photons that are scattered away from the volume, may be re-scattered back towards it. The* ***c****-photons scattered at a small angle may still end up in the same volume, and the* ***d****-photons that would not end up in the volume if not scattered can be directed towards it through a scattering event.*

The light that is scattered in the measurement volume in the direction towards the camera is attenuated also after the scattering event, by particles in between the scattering volume and the collection lens. As for the attenuation of the laser light, this attenuation can be described by the Beer-Lambert law, given that the MS can be rejected.

4.2 Multiple scattering suppression

As already mentioned, the multiple scattered light can be separated from the light that is only scattered once by introducing a spatial intensity pattern in the laser sheet. The technique is commonly referred to as *structured laser illumination planar imaging* (SLIPI). The basic idea is that if the modulation is sufficiently fine, the multiply scattered light loses the spatial modulation whereas it is preserved in the light that is scattered only once. Commonly, three images in which the sinusoidal intensity

modulation is shifted in respect to each one another a third of the modulation period are recorded. The data in which the multiply scattered light has been suppressed, can be calculated as

$$S_{SS} = \frac{\sqrt{2}}{n}\left[\sum_{j=1}^{n-1}\sum_{k=j+1}^{n}(S_j - S_k)\right]^{1/2}. \tag{4.5}$$

Here, S_{SS} refers to the single scattered light and S_{1-3} are the images recorded at different phase shifts of the spatial modulation in the illumination. If conventional laser sheet imaging is used, the MS light is not suppressed. Such a result can be simulated by adding up the recordings from the three images of the modulated illumination in accordance with

$$S_C = \frac{1}{n}\sum_{j=1}^{n} S_j. \tag{4.6}$$

Thus, the detected signal originating from MS light can be expressed as

$$S_{MS} = S_c - S_{SS}. \tag{4.7}$$

In the top row in Fig. 4.2 the images display the recording of the light scattered by particles immersed in water in a cuvette. The illuminating laser sheet is spatially modulated in a sinusoidal pattern at three different phases. In comparing the position of the intensity maxima in the images, one can note that the modulation is shifted one third of a period between successive images. Based on these data and Eqs. (4.5) to (4.7), images of the *conventional* data, the single scattered light and the MS light are reconstructed, their being printed in the bottom row of Fig. 4.2. Note that the signal is stronger in the right part than in the left part of the cuvette, both in the raw images and in the *conventional* image, despite the fact that the laser sheet enters from the left side. This can be explained by the fact that the probability of the light being scattered in the forward scattering lobe, for the current particle size, index of refraction and laser wavelength, is much greater than that of side scattering occurring. Since it takes a a number of scattering events within the forward scattering lobe for the photons to turn out towards the detector, the MS light detected is stronger on the exit side of the cuvette. Another noticeable feature is the small region of high intensity signal that can be seen close to the top at the right side of the cuvette in all of the images except the SLIPI image. This is an artifact due to light being scattered by dust on the exit surface of the cuvette, the light being filtered out in the SLIPI process.

4.3 Calculation of the extinction coefficient

With the MS light being suppressed by means of SLIPI, the attenuation of the laser light and the signal light behaves in accordance to the Beer-Lambert law (Eq. (4.4)). A brief account of how this can be utilized in order to calculate the local extinction coefficient throughout the spray will be given here. A more detailed account of it can be found in Paper III. The basic idea is to record the scattered signal as the laser sheet is scanned though the spray. Since at the outskirts of the spray, facing

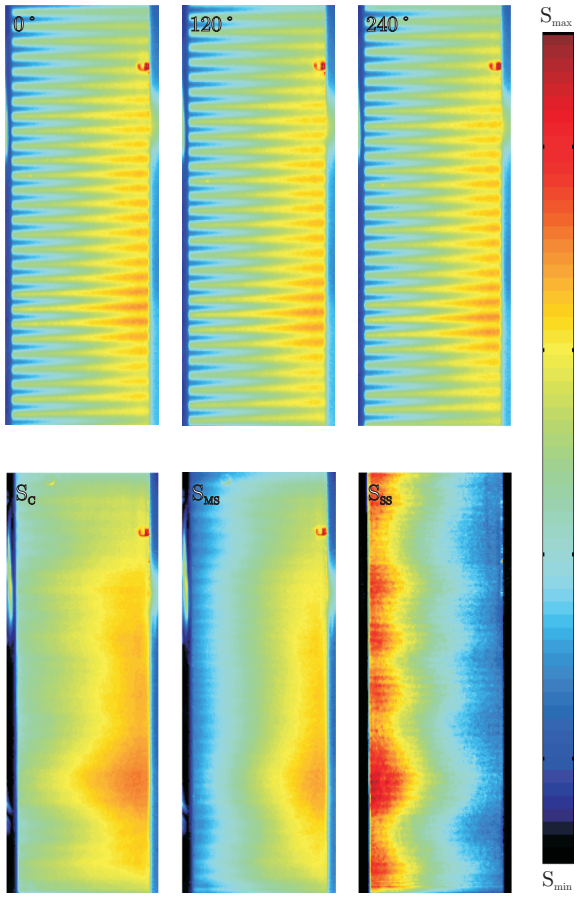

Figure 4.2: *A cuvette with* 0.5 µm *monodisperse polysterian spheres dispersed in water, illuminated by a modulated laser sheet* ($\lambda = 532$ nm) *entering from the left side* 5.5 mm *from the cuvette surface facing the camera. The top three images are the recorded data for three different phases of the modulation. The bottom three images are the calculated conventional image,* S_c*, the MS image,* S_{MS}*, and the SLIPI image,* S_{SS}*.*

the detector, the light scattered towards the detector is not attenuated by the spray, the signal attenuation can here be neglected. If the incident irradiance is measured, the intensity of the detected light that was scattered on the first droplets can be related to the magnitude of the attenuation of the laser light at that point. The attenuation that was calculated here enables the irradiance of the laser light at the next scattering event to be calculated. This can be repeated in the direction of the laser sheet throughout the spray. With the irradiances calculated, the extinction coefficient can be extracted by use of the Beer-Lambert law (Eq. (4.4)). As the laser sheet is scanned deeper into the spray, the scattered light attenuated on its path towards the detector. The already calculated extinction coefficients in this region can be used then to compensate for the attenuation of the signal.

In the region closest to the detector, where the signal attenuation can be neglected, the integrated signal is related to the integrated attenuation of the laser light (measured on the basis of the difference in irradiation before and after the spray) in the same way as the local signal is related to the local attenuation.

$$\frac{I_i(y,z) - I_f(y,z)}{\int_0^\infty S_{ss}(x,y,z)dx} = \frac{I(x,y,z) - I(x+\delta x,y,z)}{\int_x^{x+\delta x} S_{ss}(x',y,z)dx'}, \tag{4.8}$$

where δx is the width of the area imaged onto one pixel in the detector and $I_i(y,z)$ and $I_f(y,z)$ are the initial and the final irradiance, respectively. If the local irradiances, expressed in the numerator at the right-hand side of Eq. (4.8), are instead expressed with use of the Beer-Lambert law (Eq. (4.4)), it becomes

$$\frac{I_i(y,z) - I_f(y,z)}{\int_0^\infty S_{ss}(x,y,z)dx} = \frac{I_i(y,z)\mathrm{e}^{-\int_0^x \mu_e(x',y,z)dx'}\left(1 - \mathrm{e}^{-\int_x^{x+\delta x} \mu_e(x',y,z)dx'}\right)}{\int_x^{x+\delta x} S_{ss}(x',y,z)dx'}. \tag{4.9}$$

To translate Eq. (4.9) into something that can be related to the signal detected by a camera detector, consider Fig. 4.3. The signal recorded by the detector does not have

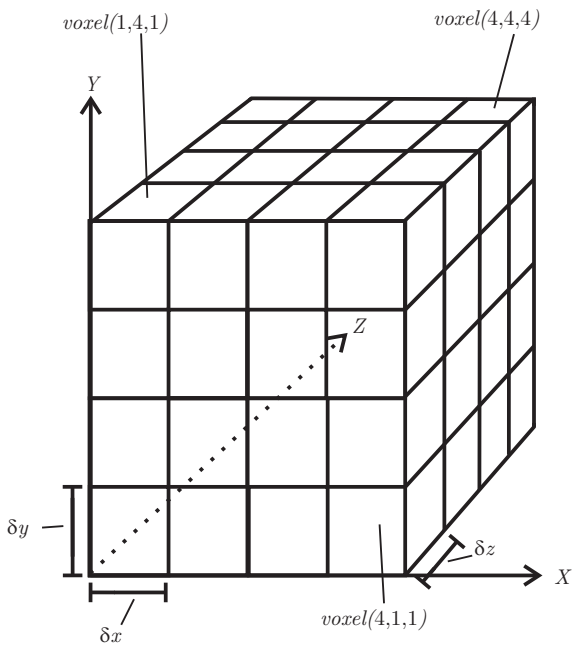

Figure 4.3: *Illustration of how the measurement volume can be divided into voxels. Each voxel is spanned by an area the size of a detector pixel in the image plane $\delta x \times \delta y$, times the distance between two adjacent positions of the laser sheet in the depth scan δz.*

infinitesimal resolution, as would be required to compute the integrals in Eq. (4.9). At best, it is limited by the size of the pixels in the imaging plane (δx and δy) and the distance between the laser sheets in the depth scan, δz. We define $\overline{S}_{ss}(k,l,m)$ and

$\bar{\mu}_e(k,l,m)$ now as being the average SLIPI signal and extinction coefficient within the volume $\delta x \times \delta y \times \delta z$, located at (k,l,m), where (k,l,m) represents the voxel number in the direction of (x,y,z). Replacing the integrals in Eq. (4.9) by summations over the voxels results in

$$\frac{I_i(l,m) - I_f(l,m)}{\sum_{k=0}^{k_{max}} \bar{S}_{ss}(k,l,m)} = \frac{I_i(l,m) \mathrm{e}^{-\sum_{k'=0}^{k} \mu_e(k',l,m)\delta x} \left(1 - \mathrm{e}^{-\mu_e(k+1,l,m)\delta x}\right)}{\bar{S}_{ss}(k,l,m)}. \tag{4.10}$$

Assume now that the absorption cross-section is negligible in comparison to the scattering cross-section. The loss in irradiation over a voxel, as given in the nominator on the right hand side in Eq. (4.8), then is equal to the scattered irradiation $\bar{I}_{ss}$

$$\bar{I}_{ss}(k,l,m) = \bar{S}_{ss}(k,l,m) \frac{I_i(l,m) - I_f(l,m)}{\sum_{k=0}^{k_{max}} \bar{S}_{ss}(k,l,m)}. \tag{4.11}$$

Rearranging Eq. (4.10) and using the expression of the scattered irradiation given in Eq. (4.11) allows the average extinction coefficient within a voxel to be expressed as

$$\bar{\mu}_e\left((k+1),l,m\right) = -\frac{1}{\delta x} \ln\left(1 - \frac{\bar{I}_{ss}(k,l,m)}{I_i(l,m)\mathrm{e}^{-\sum_{k'=0}^{k} \bar{\mu}_e(k',l,m)\delta x}}\right). \tag{4.12}$$

Since the extinction coefficient is required for calculating the attenuation of the laser sheet up to the position at which the extinction coefficient is to be calculated, Eq. (4.12) must be used one pixel column at a time in the direction of the laser sheet.

As already mentioned, Eq. (4.12) is only valid if the attenuation of the signal light can be ignored, as in the outermost part of the spray closest to the detector. Further into the spray, the signal attenuation needs to be taken into account. Fortunately, when the extinction coefficient has been calculated in the plane closest the camera, the attenuation of the signal light that propagates through this plane can be calculated. By taking the signal attenuation into account, the irradiance scattered from a given voxel can be expressed as

$$\bar{I}_{ss}(k,l,m) = \frac{\bar{S}_{ss}(k,l,m)}{\sum_{m'=0}^{m-1} \mathrm{e}^{-\bar{\mu}_e(k,l,m')\delta y}} \frac{\left(I_i(l,m) - I_f(l,m)\right)}{\sum_{k=0}^{k_{max}} \sum_{m'=0}^{m-1} \frac{\bar{S}_{ss}(k,l,m)}{\mathrm{e}^{-\bar{\mu}_e(k,l,m')\delta y}}}. \tag{4.13}$$

Thus, with the expression of the scattered irradiation according to Eq. (4.13), Eq. (4.12) can be used to calculate the extinction coefficient within the entire spray.

4.3.1 Sensitivity to multiple scattering residuals

The validity of the calculation of the extinction coefficient by use of Eq. (4.12) is dependent upon the light attenuated following the Beer-Lambert law. This in turn is only true if the multiply scattered light is fully suppressed. Although most of the MS

light is suppressed in the SLIPI approach, some residuals are always present. This is especially true in dense media containing large particles [59].

Due to the MS residuals that are present in the $\overline{S}_{ss}$ data, the extinction coefficient is overestimated in the parts of the image that contain more MS residuals and is underestimated in the parts containing less. Let us say that the extinction coefficient in the central part of the cross-section located closest to the camera (that is calculated first) is overestimated in this way. In the next layer the attenuation of the signal light propagating through the central part is then overestimated as well due to the overestimated extinction coefficient in the first layer. Thus the extinction coefficients in this layer may be overestimated, due both to the MS residuals in the signal from the same layer and to the overestimated extinction coefficient in the first layer. In this way, a small error in $\overline{S}_{ss}$ due to residuals of MS can induce a large error in calculation of the extinction coefficient in parts of the spray in which the signal attenuation is significant.

If the particle distribution is known, the efficiency of MS suppression by means of SLIPI can be estimated by comparing the attenuation of the light with the exponential decay predicted by the Beer-Lambert law [59]. However, if the particle distribution is unknown, this is not a feasible approach. For such cases, one should consider instead the camera function c, as expressed in Eq. (4.3). The camera function relates attenuation-corrected scattered light to the detected signal in accordance with

$$c = \frac{\overline{S}_{ss}}{\bar{I}_{ss} \sum_{m'=0}^{m-1} \mathrm{e}^{-\bar{\mu}_e(k,l,m')\delta y}}. \tag{4.14}$$

Its value depends upon such factors as the solid angle of collection, the objective transmission, the camera fill factor, the quantum efficiency and the ADC properties. Since all of these factors are held constant during an experiment, c should stay constant throughout the measurement volume. However, if the extinction coefficient is overestimated due to residuals of MS-light in $\overline{S}_{ss}$, this fact is reflected in an increase in the calculated camera function as a function of the total attenuation of the signal. In Paper III this relationship is analyzed and a suggestion of how it can be used to further suppress the MS residuals in $\overline{S}_{ss}$ in order to increase the accuracy of the calculation of $\bar{\mu}_e$ is given.

4.4 Results

In Fig. 4.4 the conventional data, the SLIPI data, and the calculated extinction coefficient from a water spray having a nominal droplet diameter of 15 µm (as given by the manufacturer) and an optical depth of up to $OD = 3$, is given. In the *conventional* image, S_c (column at the left in Fig. 4.4), the spray appears symmetric. On the basis of this data alone, it would be difficult to determine whether the detected signal is affected by MS and by the attenuation of the laser and signal light. However, in the images of the single-scattered light, S_{ss} (middle column in Fig. 4.4), the spray appears asymmetric, with the signal being shifted towards the detector and the entrance side of the laser sheet (compare with the lines drawn through the center of the spray). Thus, the scattered signal and the light in the laser sheet are in fact attenuated as they

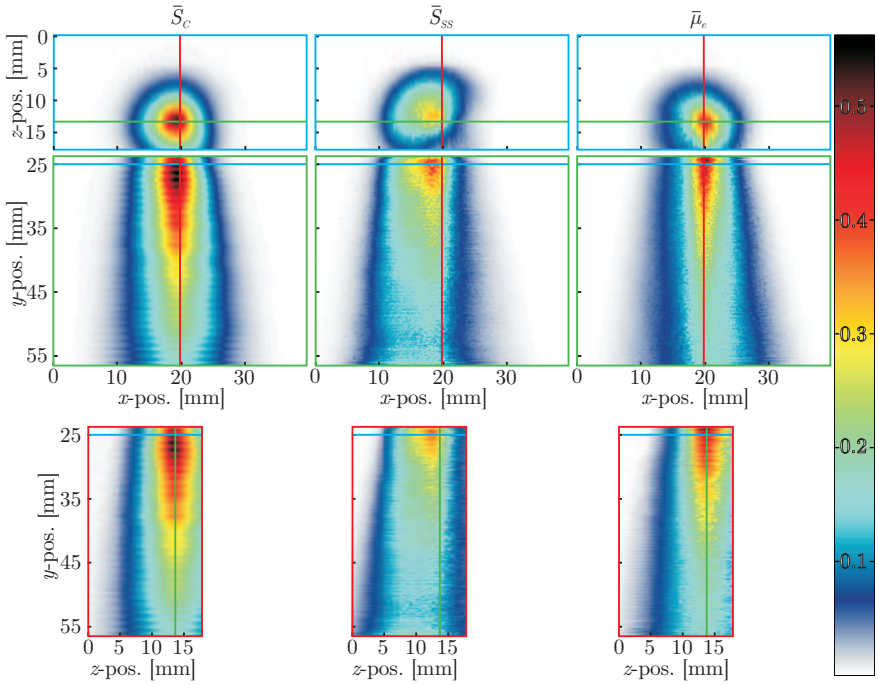

Figure 4.4: *From left to right, images of $\bar{S}_C$, $\bar{S}_{SS}$ and the $\bar{\mu}_e$ are plotted. In the top row, horizontal cross-sections are given. In the middle and bottom rows, vertical cross-sections facing the detector and the direction of the laser sheet, respectively, are displayed. In the top and middle rows, the laser sheet enters from the left and in the bottom row it is oriented perpendicular to the cross-sections. The overlaid colored lines in the respective images indicate the positions of the cross-sectional planes displayed in the images with frames of the same colors. The numbers in the color bar represent $\bar{\mu}_e$ in* $[\mathrm{mm}^{-1}]$.

propagate through the spray, the effects of MS and of attenuation thus counteracting each other in the conventional data. In comparing the conventional image with the calculated extinction coefficient, it becomes evident that the shape of the spray images are different. Thus the fact that the *conventional* signal is symmetric is no guarantee that the MS and the light attenuation can be neglected and that the data can be treated as qualitative.

In the horizontal cross-section of the calculated extinction coefficients (top row, right column in Fig. 4.4), it can be noted that the center part of the spray has a tendency to extend in the direction away from the detector. This is probably due to residual MS light, which despite further suppression, guided by the trend present in the camera function (as discussed in section 4.3.1 and detailed in Paper III), induces an artificial overestimation of the extinction coefficient in the parts of the spray having high attenuation. Further research is required for quantifying the accuracy involved and how it is affected by the properties of the spray and of the experimental setup.

Chapter 5

Challenges for in Cylinder Laser-based Combustion Diagnostics

Fossile fuel is the major energy source in the world, a growing transport sector as the largest consumer of it [2]. To increase the efficiency and decrease the pollution involved it is important to understand the combustion process. For this, laser-based optical diagnostics – with the ability to measure temperatures, flows and species concentration at a high temporal and spatial resolution – have been proven to be versatile tools [5]. However, even if an optical diagnostic technique works satisfactorily in a laboratory environment, the transition to more realistic environments, such as IC engines, may be far less than trivial. The elevated and time-varying pressure and temperatures increases the influence of quenching in measurements of LIF [61]. Pressure fluctuations induce beam steering [49]. Soot present in the combustion chamber and deposited on windows attenuate both the illuminating laser and the signal light. The limited optical access sets restrictions on the regions in the combustion chamber that are accessible, the windows required for optical access also inducing optical aberrations in the imaging system. Also, there is a risk that the windows break due to thermal gradients or high laser flux.

In this chapter, the challenges encountered while conducting laser-based optical diagnostics in IC engines during the work reported in the thesis are addressed. First the optical aberrations, induced by the curvatures in the optical widows are taken up, both in terms of image distortions – which can be removed by a transfer function employed during image post-processing – and reduction of the spatial resolution, that needs to be dealt with by use of correction optics. Following that, attenuation of the laser sheet and signals due to absorption in the combustion chamber and in the window deposits are discussed. Distortions in the signal due to gradients in the index of refraction are also exemplified. Finally, the experimental challenges associated with high-repetition-rate laser-induced incadecsence (LII) measurements in IC engines, as conducted in the studies reported in Paper V and Paper V, are highlighted.

5.1 Optical aberrations

Optical access in IC engines can be achieved either through endoscopes [62], through optical fibers [63], or by replacing some of the metal by a transparent material, such as quartz or sapphire. To access a view in the direction of the cylinder bore, either one of the exhaust gas valves or the piston crown (as in Paper V) can be replaced by a window [64]. Often flat piston crowns are used to reduce optical aberrations. However, when the requirements for emulating the real combustion process are high, more realistic shapes (that unfortunately distort the image) may be used. For side views, the top part of the cylinder liner is replaced (as in Papers IV and V), or windows are inserted (as in Paper VII). Windows can withstand larger temperature- and pressure gradients than transparent liners can and are not as expensive to replace when they break. However, the optical access is more limited. The inner surface of a liner window may be flat for minimal optical aberrations, or be made so as to follow the curvature of the cylinder liner in order to minimize the intrusiveness to the combustion geometry. A curved inner surface also acts as a negative lens, effectively increasing the field of view.

The distortions induced by curved surfaces of the optical components can, to a certain degree, be compensated for in the post-processing of the images. The general procedure there is to introduce a known grid pattern at the position of the laser sheet in the combustion chamber. By comparing coordinates in the image of the grid with the real positions, a transfer function can be constructed that relates the distorted image to an undistorted representation of the reality involved. In Fig. 5.1, the image of a distorted and of the corresponding recovered grid pattern in a IC engine viewed through a curved window are shown.

When the inner surface of a liner window is curved, the image is not only distorted in terms of an inhomogeneous horizontal demagnification, as shown on Fig. 5.1, but it also affects the horizontal focus, introducing astigmatism, with blurry images as a result. The astigmatism can be compensated for by introducing a positive cylindrical lens in front of the detector. The optimal focal strength of the cylindrical lens depends on the positions and properties of it and of all of the other optical components in the system. This is complicated to calculate analytically, and is preferably simulated using ray tracing. Ray tracing is a simple way of simulating how light is refracted through an optical system by modeling the light as rays. In a perfect imaging system, all rays originating from a given point in the object plane should end up at the same position in the image plane. Those that do not, contribute to optical aberrations in the system. With use of ray tracing it is possible to identify the aberrations and to find correction optics that remove them. In order to model the path of the rays in the system, the refraction of light at the surfaces is calculated from the law of refraction

$$n_1 \sin(\theta_1) = n_2 \sin(\theta_2), \tag{5.1}$$

where n_1 and n_2 are the indexes of refraction of the two materials responsible for the surface and θ_1 and θ_2 are the incident and the refractive angle, respectively. In Fig. 5.2 this has been done with and without a cylindrical lens to correct for the astigmatic aberration. The detector is here not placed perpendicular to the laser sheet but at an angle that extends the field of view to the entrance window of the laser sheet. To align the image plane with the laser sheet, the objective is thus tilted. In the insets

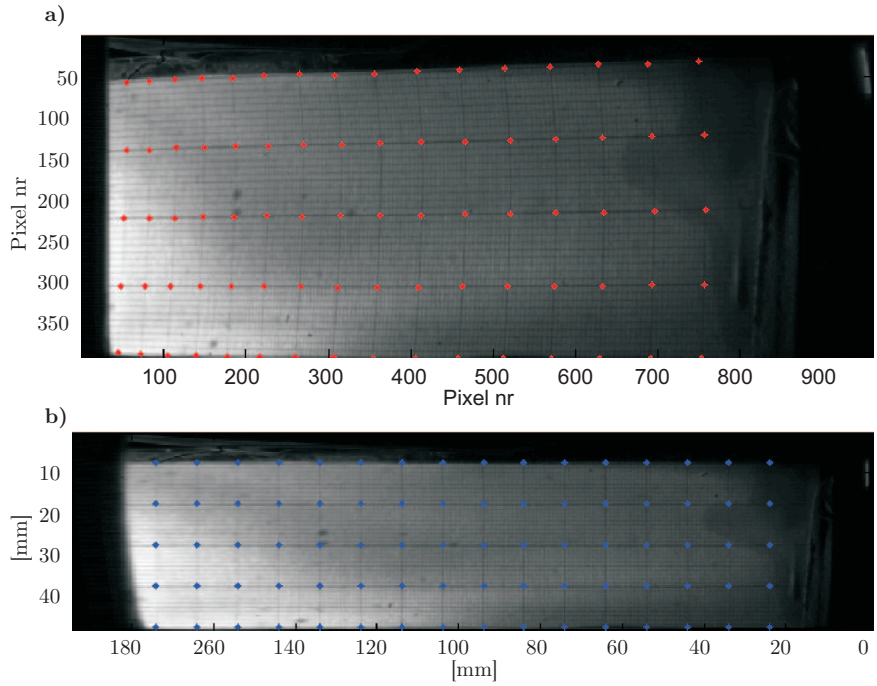

Figure 5.1: ***a*** *raw image of a grid pattern in a cylinder with identified coordinates.* ***b*** *transformed image.*

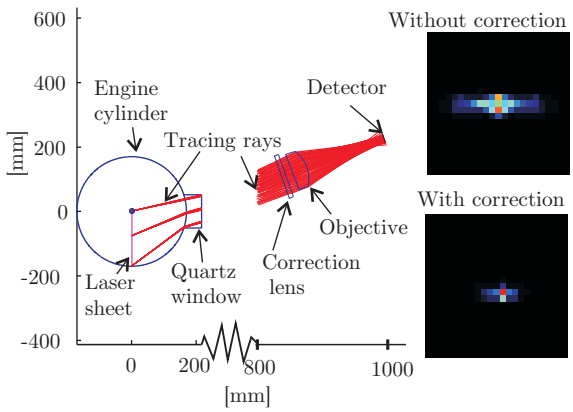

Figure 5.2: *Ray-tracing of the laser-induced fluorescence imaged through a window with a curved inner surface. Three point sources are simulated, the insets showing the resulting images of one of these points, with and without use of the correction lens.*

to the right in Fig. 5.2 the point spread function (PSF) at different positions in the image plane is given. With use of the correction lens the PSF becomes symmetrical and can thus be made smaller, effectively improving the spatial resolution.

5.2 Signal attenuation and beam steering

In addition to the attenuation of laser and signal light in an open measurement volume, as discussed in Chapter 4, a common problem when conducting measurements in IC engines is fouling of the windows as soot and oil are deposited on the surfaces during operation. A common solution is to run the engine with dry piston rings and under non-sooting conditions. However, when the engine does not have a piston extension, as in the study reported in Paper VII, or when it is the soot formation or oxidation that is to be studied, as in Paper V, these solutions are not applicable. Instead, a cleaning interval – based on the rate of window fouling and the tolerable error margin – is scheduled, the engine being disassembled and cleaned accordingly.

If possible, a measurement of the fouling that has occurred up until the time of the data recording should be carried out. This would increase the accuracy and prolong the cleaning intervals considerably. By measuring the throughput of a known signal, e.g. the homogeneous charge distribution in a premixed gas engine (as reported in Paper VII), the artifacts due to fouling can be canceled out in the post processing. If this is done, the windows do not have to be cleaned until the attenuation of the signal has reduced the S/N to a level below what is required for a reliable data evaluation to be to performed. In Fig. 5.3 this approach of removing the artifacts introduced by window fouling is illustrated. The data there was recorded in a large-

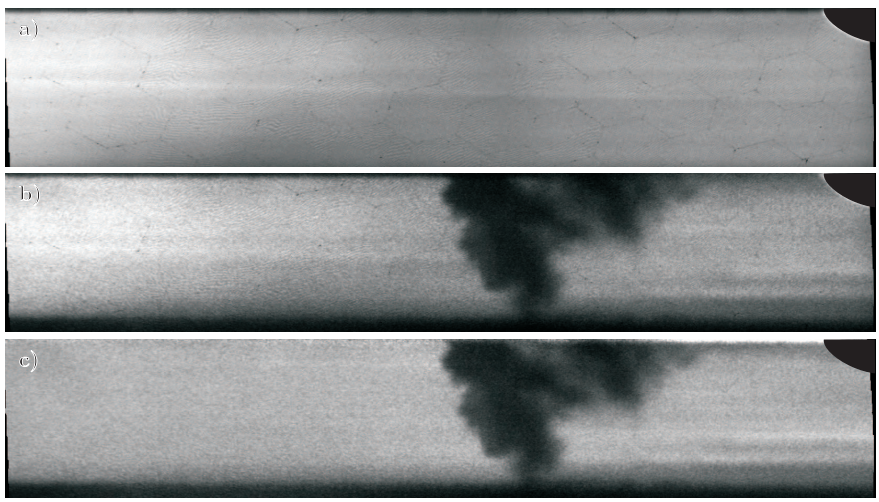

Figure 5.3: *Images of acetone LIF recorded from a large bore natural gas engine. The fluorescing acetone is premixed with the fuel. Thus the dark areas represent the regions of burnt gas. The masked quarter circle in the top right corner is part of the pre-chamber, where the combustion is initiated, and from where a burning jet propagates to the main chamber to ignite the main charge. In* ***a****, the data have been recorded prior ignition.* ***b*** *is recorded at a timing of the combustion cycle where the burning jet has propagated almost half the distance to the cylinder liner.* ***c*** *is the same data as in* ***b*** *but compensated for laser and signal attenuation by division with* ***a****.*

bore spark-ignited gas engine. To avoid knocking, such engines are operated under lean conditions. This introduces problems, however, in the igniting of the charge. To

enable reliable ignition to be carried out, the combustion chamber is divided into two parts: the pre-chamber (the masked area at the upper left in Fig 5.3 **a-c**) and the main-chamber. The much smaller pre-chamber is fueled separately by a richer fuel mixture that can be ignited by a spark plug in the pre-chamber. The ignited energetic gas-jets are pushed out through holes in the pre-chamber into the main-chamber to ignite the lean main-chamber gas. In Fig 5.3 **a**, the acetone-seeded charge is excited prior to ignition. Here the charge is distributed homogeneously, any inhomogeneities in the signal being due to attenuation of the light or to an uneven spatial energy profile of the laser sheet. The laser sheet enters the image from the left. Thus, the attenuation can be observed as a decrease in signal from left to right. At the center of the image there is a dip in the signal intensity that cannot be attributed to attenuation of the light in the laser sheet, since it increases again to the right. Instead this dip can be attributed to uneven fouling of the liner window. The data in Fig. 5.3 **b** is recorded 7 crank angle degrees (CAD) after ignition. At this point in time, the burning jets from the pre-chamber have already propagated for some distance in the main-chamber and can be seen as a black cloud (absence of signal). The stripes in the image, that are due to inhomogeneities in the laser sheet, can still be seen, along with attenuation of the laser sheet and of the signal due to fouling of the window. Additional stripes to the right of the flame jet can also be noted. These are due to variations in the index of refractions caused by the temperature gradients in the flame. In Fig. 5.3 **c** the data from Fig. 5.3 **b** have been divided with the data in Fig. 5.3 **a**. As can be seen, the artifacts introduced by the inhomogeneities in the laser sheet and the attenuation of it and due to the window fouling have been removed. Also, the honeycomb pattern – that can be seen in Fig. 5.3 **a-b** and is an artifact introduced by the bundling of the optical fibers in the coupling between the image intensifier and camera – has been removed. What is not removed, are the stripes to the right of the flame jet, since these were caused by the thermally introduced refraction of light in the laser sheet and was thus not present when the flame jet was lacking. One can also note that the flame jet seem to have a sharper gradient at the leading edge of the jet than it does closer to the pre-chamber. This is because the light emitted closer to the pre-chamber has to propagate through thermally inhomogeneous regions created by the next jet pointing in a direction intersecting the optical path.

5.3 High repetition rate LII

The yellow light seen in sooty flames originates from hot soot particles that exhibit incandescence due to the elevated flame temperature there. By intersecting the flame with a laser sheet, the temperature of the illuminated soot particles is increased further. At higher temperatures the radiant emittance from the soot particles is blue shifted and can be separated from the background light by spectral and temporal filters. Since soot particles have broad absorption spectra, the excitation wavelength can be chosen arbitrarily. However, to avoid interference from LIF, longer wavelengths are preferable. The fundamental output from an Nd:YAG at 1064 nm is a common choice.

There is an upper limit of the soot particle temperature at ~4000 K [65], a limit which is reached when the temperature increase due to absorption is balanced out by the enhanced sublimation at the surface of the particles. Thus, at high laser

fluence, the laser light affects the size and morphology of the soot particles. For single measurements, this offset is acceptable, since it is constrained to the moment of the measurement. However, if multiple measurements are conducted within a short period of time, there is a risk of each successive measurement being affected by the previous ones. Figure 5.4 shows the LII response of an MCKenna burner flame illuminated by eight laser sheets with spatial top hat energy profiles at 150 mJ/cm^2, each of them separated from the next by 139 µs (corresponding to 1 CAD in an engine operated at 1200 revolutions per minute (rpm)). The response decreases for

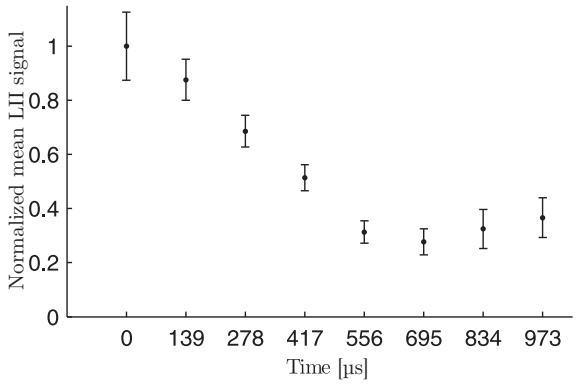

Figure 5.4: *Normalized LII signal from a MCKenna burner flame illuminated by a train of eight laser sheets with top hat spatial energy profiles, separated by* 139 µs *each. The error bars represent the standard deviations.*

each exposure due to sublimation of the soot particles, until it stabilizes finally at ~30 % of the initial value. In the MCKenna burner flame, the flow rates are slow in comparison to the flows in an IC engine. The time it would take to exchange the gas in the 1 mm thick measurement volume at the flow rates provided by the MCKenna burner corresponds to 20 ms, a time thus much longer than the 139 µs time separation of the laser exposures. With the uneven stochastic soot distribution present, Fig. 5.4 is difficult to reproduce in an IC engine. Accordingly, Fig. 5.5 shows the total LII signal from two sets of eight consecutive pulses. If the sublimation was a problem, there would be a sudden jump in the trend, going from the last laser pulse in the first burst to the first laser pulse in the second burst. As no such jumps can be seen, one can conclude that the sublimation is not as big of a problem in IC engines as in a laboratory flame having lower flow rates. For the gas to be fully exchanged in the measurement volume between two exposures (139 µs) it must flow at a rate of at least 7 m/s perpendicular to the laser sheet. In view of the flow rates there tend to be in an IC engine [66], it is a reasonable assumption that the convection mask the effect of sublimation in the IC engine.

The effects of sublimation on the LII signal can also be seen in Fig. 5.6. Here the strength of the LII signal is plotted as a function of laser fluence obtained for different spatial energy profiles in the laser sheet. The black curve marked by circles represents data from a top hat profile. As seen, the LII increases with an increase in laser fluence up to ~150 mJ. At this point, the increase in heat due to the increased laser absorption is canceled out by the increased sublimation. If the fluence is increased still further,

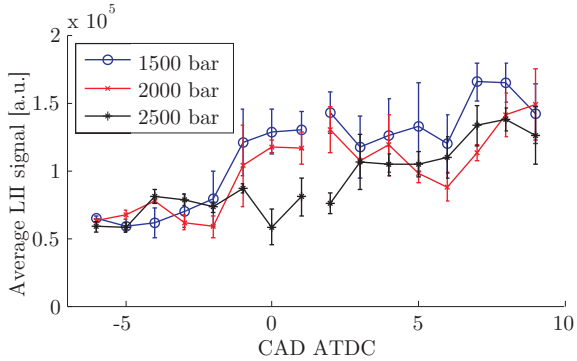

Figure 5.5: *The total LII signal at different engine timings for three different injection pressures. The eight exposures during a single combustion cycle are set to two different timings, as indicated by a gap in the curve connecting the data points. Each data point represents four to eight measurements, the standard deviation being given by the error bars.*

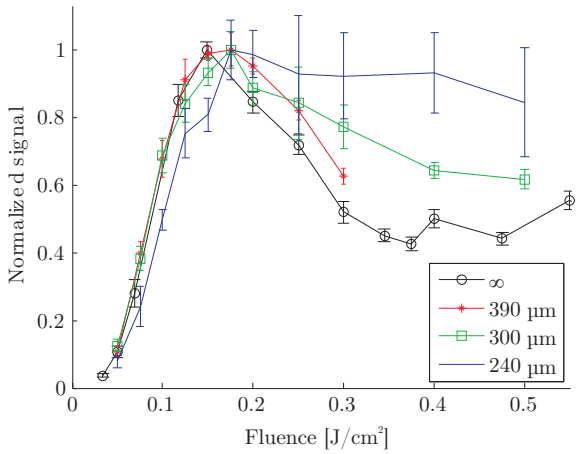

Figure 5.6: *Normalized LII signal as a function of fluence for different laser sheet profiles. A top hat energy profile, represented by the black curve, is formed by imaging an aperture to the measurement region. In order to shift the profile towards a Gaussian shape the laser sheet is focused through an aperture, effectively removing the high frequency components. The size of the aperture is given in the legend.*

the enhanced sublimation has a larger effect than that of the increased laser heating. Consequently, the LII signal decreases. It has been shown that by modifying the energy profile of the laser light it is possible to shape the fluence curve to better suit the experimental requirements [67]. To produce the curves shown in Fig. 5.6, the laser sheet was focused through a slit of varying width. As the slit was narrowed (slit widths are given in the legend), the higher orders in the spatial frequencies were removed, transforming the top hat profile into a Gaussian profile. For a Gaussian laser sheet, a reduction in the LII signal from the center of the sheet in response to an increase in fluence due to sublimation was compensated for by an increase in LII in the wings, where the sublimation is small. For the smallest slit width, represented by the

blue curve, the signal reached a plateau value. This is desirable since it then becomes insensitive to fluctuations in the laser fluence and to attenuation of the laser light in the measurement volume. Note also that the error bars are substantially larger in the data recorded at the smallest slit width than in the other data sets. This is due to small vibrations in the setup or to instabilities in the laser sheet that induce large differences in fluence and in sheet profile when combined with a narrow slit. For measurements inside IC engines, vibrations are inevitable, preventing use of such an approach. This is the case for the studies reported in Paper V and Paper VI, where the original top hat spatial profile instead is kept. Here, the fluence is adjusted to a level just above the peak LII value, where the response to changes in fluence is small. Thus, small fluctuations in the laser fluence due to laser instabilities or to attenuation have little effect on strength of the signal. However, under sooty IC engine conditions the laser attenuation may be large enough to still effect the signal level appreciably. In Fig. 5.7 the soot is illuminated by a laser sheet with a top hat spatial energy

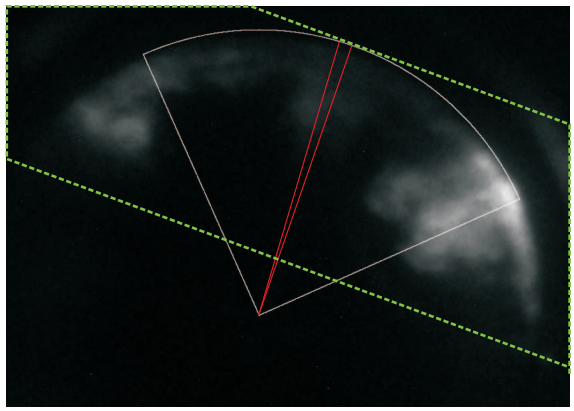

Figure 5.7: *The average LII signal from 24 images recorded between 6 and 8 CAD after top dead center. The circle sector is centered around the illuminated spray (indicated by the red lines). It covers the spray and recirculation zones. The laser sheet enters from the lower right portion of the image and exits in the upper left corner. The illuminated volume is shown by a dotted line.*

profile and an initial fluence of $200\,\mathrm{mJ/cm^2}$, corresponding to a position just right of the peak in the black curve shown in Fig. 5.6. The signal from the recirculation zone to the left of the spray is lower than that from the recirculation zone to the right of it, despite that, since the figure shows an average of 24 images the soot concentration should appear symmetric. This difference is most probably due to laser attenuation.

Chapter 6

Summary and Outlook

To conclude the work presented in the thesis, laser based optical diagnostic techniques were developed and/or improved so as to be able to include the temporal and third spatial dimension, reduce uncertainties, and enable quantification of the data. In parallel to seeking answers to combustion related questions, the challenges associated with applying existing measurement techniques to IC engines were addressed.

Mie scattering and PLIF – commonly used for collecting two-dimensional data – were extended to the temporal and the third spatial dimension by combining a high-repetition laser and a detection system making use of oscillating mirrors. The oscillations from two mirrors, operated at different frequencies and phases were combined in order to achieve more equally spaced measurement planes. Post-processing methods enabling flame fronts and OH-concentrations to be calculated in the massive data sets involved here were described.

By introducing a spatial modulation to the illumination, the contribution of multiple scattered light to the signal was suppressed. A method was developed enabling the laser and signal attenuation to be calculated so as to be able to extract the local extinction coefficient from the data for the single-scattered light. To verify the method, it was applied on a homogeneous distribution of scattering particles. The method was also applied to a spray, the result being compared with those for conventional planar illumination. A method for detecting and further suppressing residuals of multiple scattered light that had not been successfully removed by the spatial modulation in the illumination, was also developed.

A variety of measurement techniques, including Mie scattering, PLIF and LII were applied to IC engines (light- and heavy-duty diesel engines and a large bore gas engine). Conclusions regarding fuel spray propagation and soot formation in diesel engines and jet formation in pre-chamber-ignited gas engines were drawn. By use of the same measurements, challenges associated with limited optical access, a harsh environment and high repetition rates were addressed. Optical aberrations were dealt with in the image post-processing and by correction optics developed using ray tracing. Artifacts due to attenuation of the laser sheet, window fouling and beam inhomogeneities were identified and were suppressed by measurements in a homogeneous environment. The effect of laser induced soot sublimation during

time-resolved LII measurements were investigated in atmospheric flames and in IC engines.

The following recommendations are given for future work:

- *Proper investigation of the limits to optical depth in calculation of the extinction coefficient, and of how the camera function varies.*
  Success in calculation of the extinction coefficients, as presented in Paper III, is dependent upon the efficiency of suppressing the MS light. If it is not properly suppressed, the calculated camera function will vary as a function of the depth position in the spray (although this, in fact, should be constant). If the relationships involved are clarified, the calculated camera function can be used to estimate both the accuracy of the calculated extinction coefficient and the efficiency of the suppression of the MS.

- *Extend the measurement technique presented in Paper III to include particle size distribution and concentration*
  By combining a measurement of the extincion coefficient with measurement of the particle size distribution using the LIF/Mie ratio technique, both particle size and concentration distribution can be deduced.

- *Adaptation of the algorithm for calculating the extinction coefficient to LIF*
  The approach of calculating the extinction coefficient by relating measurements of transmission to the strength of the recorded Mie scattering, as was done in Paper III, could be extended to absorbing and fluorescing material. This was employed in Paper II, but without implementation of the re-absorption of the fluorescence. The reason for this is that the fluorescence, in contrast to the Mie scattering, is not proportional to the absorption, due to variations in the collisional quenching. In addition, the absorption coefficient is not the same for the emitted light, that origin from a temperature dependent distribution of transitions, as for the laser light, that target a single temperature-insensitive transition. However, if the temperature and the quenching can be measured, and the measurement throughout the volume is conducted in a more instantaneous manner, such a calculation would be possible.

- *Investigation of the non linearities in the image intensifier MCP*
  Many laser-based combustion diagnostic techniques require the use of image intensifiers, mainly so as to obtain UV-sensitivity and improved temporal gating. In high repetition rate measurements, this can become problematic, due to depletion effects in the intensifier MCP. To increase the accuracy of such measurements, it would be valuable to be able to characterize the level of depletion obtained through use of a model. Such a model, if properly calibrated, could be used inversely to estimate the original signal from the unevenly amplified output. Much of this work has already been done and is presented in chapter 2.

- *Combine time resolved 3D LIF with time resolved volumetric PIV*
  If the OH A-X (0,1) transition at 283 nm rather than the (0,0) vibrational transition is targeted, it would be possible to combine 3D time-resolved measurements of OH with volumetric time-resolved PIV. The reduced absorption cross-section for this transition could be compensated for by reducing the depth

of field (through use of a larger collection angle). Such measurements would enable calculation of flame front velocities to be carried out and would provide extensive information regarding flame flow interactions.

- *Cycle-to-cycle variations in the pre-chamber ignition process*
  One of the conclusions drawn in Paper VII – in which the flame jets from the pre-chamber were studied in the main chamber – was that the main contribution to the instabilities in combustion phasing originate from the ignition process in the pre-chamber. With use of a pre-chamber made in quartz, it would be possible to follow the mixing process in the pre-chamber up until ignition, so as to be able to better understand this process.

- *Absorption compensation in LII and other means of creating a semi-Gaussian laser sheet*
  One of the major uncertainties in measurement of the LII from the IC engine, as reported in Paper V and Paper VI is caused by attenuation of the laser light. The solution pursued at that time was to to modify the spatial profile of the laser sheet by spatial filtering. However, the enhanced sensitivity to vibrations due to the filtering made this approach unsuccessful. Optional methods to re-shape the spatial energy profile – such as displacing the slit that is projected to the combustion chamber in order to create a blurred top hat profile – could be pursued. Instead of reshaping the beam profile, the beam path could be orientated for bi-directional illumination, which would almost eliminate the error from laser attenuation. Alternatively, if the total absorption were measured, an approach similar to that employed in Paper III and Paper II could be used to calculate and compensate for the laser attenuation.

Acknowledgements

The work reported in the thesis cannot be attributed to a single individual, but is the collective result of many collaborations. I would like to express here my gratitude to all of those persons who have been specifically important to me and to my work during these years.

Marcus Aldén: I am both very impressed and very grateful to you for how you managed to build a research group with such an open and productive atmosphere, and that you let me be part of it. You are always very generous with your time, regardless of how pressed your schedule may be. Your sharp mind and vast knowledge have been exceedingly valuable to me both for the progress of my projects and as a source of inspiration. By encouraging me to pursue my own ideas, you helped me keep my motivation high.

Mattias Richter: If it was not for you, I would still be focusing on one of the insignificant details that happened to catch my attention at the beginning of my PhD work. Where I manage to find the most complex solution to a problem, you see the easy one. Sometimes I listen to you and take your advise, but equally often I don't. Despite this, you have always fully supported my work, and if unable to help me directly you always know whom I should turn to.

Collaborators: I have had the opportunity to collaborate with researchers both from other divisions at the university and from industry. Regarding Jari Hyvonen at Wartsilla and Öivind Andersen at the Department of Energy Sciences, it has been great working with you. Your knowledge and eagerness to share it has been inspiring. Jeudi Duong, Ulf Aronsson, Clement Chartier and Guillaume Lequien, thank you for the fun we had in our common projects.

Coworkers I would like to thank Johan Sjöholm, Joakim Rosell, Zheming Li, Edouard Berrocal, Per Petersson and Jimmy Olofsson for all the hours we spent together in the labs and discussing research. I learned a lot from you.

Colleagues: Even without direct collaboration in the projects, I have received a great deal of help from other coworkers at the Division. Although I in one way or another involved most of the personnel employed at the Division with my problems, I would like in particular to mention Joakim Bood, Andreas Ehn,

Christian Brackman, Nils-Erik Olofsson, Malin Jonsson and Christoph Knappe. The discussions we had have been invaluable. I would also like to thank Rutger Lorensson, Igor Buzuk, Cecilia Bille and Minna Ramkull for all your technical and practical support.

I am also very grateful for all the personal support and the friendship that I have received during the years here. Although this goes for most colleagues at the division, I would like to specially mention Nils-Erik Olofsson, Christoph Knappe, Joakim Rosell, Edouard Berrocal, Emil Nordström, Johannes Lindén, Malin Jonsson, Jesper Borggren, Moah Christensen and Zheming Li. Thank you, it has been great getting to know you.

Elias Kristensson: I have a lot to thank you for. I am grateful your helping me to trick Marcus into hiring me. I am grateful that I got to work with you at the beginning of my PhD work. You are the most ambitious and determined person I know, and I am grateful for the way you inspired me. But most of all I am grateful to be your friend.

Construction workers: During my PhD work, I have had a second job, that of renovating my house. I would like to express my gratitude to those of you who helped me with this, indirectly enabling me to retain some focus on my PhD work. Thank you Jesper Borggren, Nils-Erik Olofsson, Elias Kristensson, Kristofer Thorsell and Zheming Li. Thank you Mona and Christer Svensson. Thank you, mother, father and my sisters. It is nice to have a dry and *almost* mold-free atmosphere to live in.

My wife: Finally, I would like to thank Christine Wellander. Without your support this thesis would not have been finalized. You kept me on track, gave me perspective and helped me focus on the important parts.

Bibliography

[1] T. F. Stocker et al., "Climate change 2013: the physical science basis", *Intergovernmental panel on climate change, working group I contribution to the IPCC fifth assessment report (AR5)(Cambridge Univ Press, New York)* (2013).

[2] IEA, *Key world energy statistics*, Report, 2013.

[3] IEA, *Redrawing the energy-climate map–World energy outlook special report*, Report, 2013.

[4] WHO, *Air quality guidelines: global update 2005: particulate matter, ozone, nitrogen dioxide, and sulfur dioxide*, World Health Organization, 2006.

[5] Kohse-Hoinghaus, *Applied combustion diagnostics*, New York: Taylor & Francis, 2002.

[6] M. J. Dyer and D. R. Crosley, "Two-dimensional imaging of OH laser-induced fluorescence in a flame", *Optics letters* **7**, 8 (1982), pp. 382–384.

[7] V. Sick, "High speed imaging in fundamental and applied combustion research", *Proceedings of the combustion institute* **34**, 2 (2013), pp. 3509–3530.

[8] G. Kychakoff et al., "Movies and 3-D images of flowfields using planar laser-induced fluorescence", *Applied optics* **26**, 13 (1987), pp. 2498–2500.

[9] M. Reeves et al., "A high-speed all-digital technique for cycle-resolved 2-D flow measurement and flow visualisation within SI engine cylinders", *Optics and lasers in engineering* **31**, 4 (1999), pp. 247–261.

[10] C. F. Kaminski, J. Hult, and M. Aldén, "High repetition rate planar laser induced fluorescence of OH in a turbulent non-premixed flame", *Applied physics b-lasers and optics* **68**, 4 (1999), pp. 757–760.

[11] M. J. Dyer and D. R. Crosley, "Rapidly sequenced pair of two-dimensional images of OH laser-induced fluorescence in a flame", *Optics letters* **9**, 6 (1984), pp. 217–219.

[12] B. Thurow, N. B. Jiang, and W. Lempert, "Review of ultra-high repetition rate laser diagnostics for fluid dynamic measurements", *Measurement science & technology* **24**, 1 (2013).

[13] M. N. Slipchenko et al., "All-diode-pumped quasi-continuous burst-mode laser for extended high-speed planar imaging", *Optics express* **21**, 1 (2013), pp. 681–689.

[14] N. Jiang, M. C. Webster, and W. R. Lempert, "Advances in generation of high-repetition-rate burst mode laser output", *Applied optics* **48**, 4 (2009), B23–B31.

[15] V. Weber et al., "Pixel-based characterisation of CMOS high-speed camera systems", *Applied physics b-lasers and optics* **103**, 2 (2011), pp. 421–433.

[16] J. Lindén et al., "Limitations of ICCD detectors and optimized 2D phosphor thermometry", *Measurement science and technology* **23**, 3 (2012), p. 035201.

[17] L. Giudicotti, "Time dependent model of gain saturation in microchannel plates and channel electron multipliers", *Nuclear instruments and methods in physics research section a: accelerators, spectrometers, detectors and associated equipment* **659**, 1 (2011), pp. 336–347.

[18] E. R. Hawkes, R. Sankaran, and J. H. Chen, "Estimates of the three-dimensional flame surface density and every term in its transport equation from two-dimensional measurements", *Proceedings of the combustion institute* **33**, 1 (2011), pp. 1447–1454.

[19] J. Katz and J. Sheng, "Applications of holography in fluid mechanics and particle dynamics", *Annual review of fluid mechanics*, vol. 42, Annual Review of Fluid Mechanics, 2010, pp. 531–555.

[20] K. Peterson et al., "Single-camera, three-dimensional particle tracking velocimetry", *Optics express* **20**, 8 (2012), pp. 9031–9037.

[21] C. J. Elkins and M. T. Alley, "Magnetic resonance velocimetry: applications of magnetic resonance imaging in the measurement of fluid motion", *Experiments in fluids* **43**, 6 (2007), pp. 823–858.

[22] C. Brücker and W. Althaus, "Study of vortex breakdown by particle tracking velocimetry (ptv)", *Experiments in fluids* **13**, 5 (1992), pp. 339–349.

[23] M. L. Greene and V. Sick, "Volume-resolved flame chemiluminescence and laser-induced fluorescence imaging", *Applied physics b* **113**, 1 (2013), pp. 87–92.

[24] B. Yip et al., "Time-resolved three-dimensional concentration measurements in a gas jet", *Science* **235**, 4793 (1987), pp. 1209–11.

[25] B. Yip, R. L. Schmitt, and M. B. Long, "Instantaneous three-dimensional concentration measurements in turbulent jets and flames", *Optics letters* **13**, 2 (1988), pp. 96–98.

[26] J. Nygren et al., "Three-dimensional laser induced fluorescence of fuel distributions in an hcci engine", *Proceedings of the combustion institute* **29** (2002), pp. 679–685.

[27] J. Hult et al., "Quantitative three-dimensional imaging of soot volume fraction in turbulent non-premixed flames", *Experiments in fluids* **33**, 2 (2002), pp. 265–269.

[28] K. Y. Cho et al., "High-repetition-rate three-dimensional OH imaging using scanned planar laser-induced fluorescence system for multiphase combustion", *Applied optics* **53**, 3 (2014), pp. 316–26.

[29] S. Deusch and T. Dracos, "Time resolved 3D passive scalar concentration-field imaging by laser induced fluorescence (LIF) in moving liquids", *Measurement science and technology* **12**, 2 (2001), p. 188.

[30] G. Hartung et al., "Flame front tracking in turbulent lean premixed flames usingâ stereo PIV and time-sequenced planar LIF of OH", *Applied physics b* **96**, 4 (2009), pp. 843–862.

[31] P. J. Trunk et al., "Premixed flame propagation in turbulent flow by means of stereoscopic PIV and dual-plane OH-PLIF at sustained kHz repetition rates", *Proceedings of the combustion institute* **34** (2013), pp. 3565–3572.

[32] M. Sweeney and S. Hochgreb, "Autonomous extraction of optimal flame fronts in OH planar laser-induced fluorescence images", *Applied optics* **48**, 19 (2009), pp. 3866–3877.

[33] C. M. Vagelopoulos and J. H. Frank, "An experimental and numerical study on the adequacy of ch as a flame marker in premixed methane flames", *Proceedings of the combustion institute* **30**, 1 (2005), pp. 241–249.

[34] R. J. H. Klein-Douwel et al., "CH and formaldehyde structures in partially-premixed methane/air coflow flames", *Combustion science and technology* **167**, 1 (2001), pp. 291–310.

[35] A. N. Karpetis et al., "Laser imaging system for determination of three-dimensional scalar gradients in turbulent flames", *Optics letters* **29**, 4 (2004), pp. 355–357.

[36] B. O. Ayoola et al., "Spatially resolved heat release rate measurements in turbulent premixed flames", *Combustion and flame* **144**, 1-2 (2006), pp. 1–16.

[37] H. Malm et al., "Nonlinear diffusion filtering of images obtained by planar laser-induced fluorescence spectroscopy", *Josa a* **17**, 12 (2000), pp. 2148–2156.

[38] J. Canny, "A computational approach to edge-detection", *Ieee transactions on pattern analysis and machine intelligence* **8**, 6 (1986), pp. 679–698.

[39] J. B. Michael et al., "100 kHz thousand-frame burst-mode planar imaging in turbulent flames", *Optics letters* **39**, 4 (2014), pp. 739–742.

[40] L. Piegl, "On NURBS: a survey", *Ieee computer graphics and applications* **11**, 1 (1991), pp. 55–71.

[41] E. Piepmeier, "Theory of laser saturated atomic resonance fluorescence", *Spectrochimica acta part b: atomic spectroscopy* **27**, 10 (1972), pp. 431–443.

[42] P. Andresen et al., "Laser-induced fluorescence with tunable excimer lasers as a possible method for instantaneous temperature-field measurements at high-pressures - checks with an atmospheric flame", *Applied optics* **27**, 2 (1988), pp. 365–378.

[43] P. Andresen et al., "Fluorescence imaging inside an internal combustion engine using tunable excimer lasers", *Applied optics* **29**, 16 (1990), pp. 2392–2404.

[44] N. S. Bergano et al., "Picosecond laser-spectroscopy measurement of hydroxyl fluorescence lifetime in flames", *Optics letters* **8**, 8 (1983), pp. 443–445.

[45] A. Ehn et al., "Single-laser shot fluorescence lifetime imaging on the nanosecond timescale using a dual image and modeling evaluation algorithm", *Opt express* **20**, 3 (2012), pp. 3043–56.

[46] R. Barlow, R. Dibble, and R. P. Lucht, "Simultaneous measurement of raman scattering and laser-induced oh fluorescence in nonpremixed turbulent jet flames", *Optics letters* **14**, 5 (1989), pp. 263–265.

[47] M. Versluis et al., "2-D absolute OH concentration profiles in atmospheric flames using planar LIF in a bi-directional laser beam configuration", *Applied physics b-lasers and optics* **65**, 3 (1997), pp. 411–417.

[48] H. M. Hertz and M. Aldén, "Calibration of imaging laser-induced fluorescence measurements in highly absorbing flames", *Applied physics b-photophysics and laser chemistry* **42**, 2 (1987), pp. 97–102.

[49] A. Arnold et al., "Quantitative measurements of OH concentration fields by two-dimensional laser-induced fluorescence", *Applied physics b-lasers and optics* **64**, 5 (1997), pp. 579–583.

[50] N. Chigier, "An assessment of spray technology–editorial", **3**, 4 (1993), pp. 365–371.

[51] W. D. Bachalo, "Method for measuring the size and velocity of spheres by dual-beam light-scatter interferometry", *Appl opt* **19**, 3 (1980), pp. 363–70.

[52] G. Wigley et al., "Imaging and PDA analysis of a GDI spray in the near-nozzle region", *Experiments in fluids* **36**, 4 (2004), pp. 565–574.

[53] A. R. Glover, S. M. Skippon, and R. D. Boyle, "Interferometric laser imaging for droplet sizing: a method for droplet-size measurement in sparse spray systems", *Applied optics* **34**, 36 (1995), pp. 8409–8421.

[54] M. Maeda, T. Kawaguchi, and K. Hishida, "Novel interferometric measurement of size and velocity distributions of spherical particles in fluid flows", *Measurement science and technology* **11**, 12 (2000), p. L13.

[55] C.-N. Yeh, H. Kosaka, and T. Kamimoto, "A fluorescence/scattering imaging technique for instantaneous 2-D measurement of particle size distribution in a transient spray", *Proc. 3rd int. congress on optical particle sizing* (1993), pp. 355–61.

[56] R. Domann and Y. Hardalupas, "Quantitative measurement of planar droplet sauter mean diameter in sprays using planar droplet sizing", *Particle & particle systems characterization* **20**, 3 (2003), pp. 209–218.

[57] M. C. Jermy and D. A. Greenhalgh, "Planar dropsizing by elastic and fluorescence scattering in sprays too dense for phase doppler measurement", *Applied physics b* **71**, 5 (2000), pp. 703–710.

[58] E. Berrocal et al., "Quantitative imaging of a non-combusting diesel spray using structured laser illumination planar imaging", *Applied physics b* **109**, 4 (2012), pp. 683–694.

[59] E. Kristensson et al., "Analysis of multiple scattering suppression using structured laser illumination planar imaging in scattering and fluorescing media", *Optics express* **19**, 14 (2011), pp. 13647–13663.

[60] Y. N. Mishra, E. Kristensson, and E. Berrocal, "Reliable LIF/Mie droplet sizing in sprays using structured laser illumination planar imaging", *Optics express* **22**, 4 (2014), pp. 4480–4492.

[61] C. Schulz and V. Sick, "Tracer-LIF diagnostics: quantitative measurement of fuel concentration, temperature and fuel/air ratio in practical combustion systems", *Progress in energy and combustion science* **31**, 1 (2005), pp. 75–121.

[62] U. Dierksheide et al., "Endoscopic 2D particle image velocimetry (PIV) flow field measurements in IC engines", *Experiments in fluids* **33**, 6 (2002), pp. 794–800.

[63] T. Husberg et al., *Piston temperature measurement by use of thermographic phosphors and thermocouples in a heavy-duty diesel engine run under partly premixed conditions*, Report, SAE Technical Paper, 2005.

[64] F. W. Bowditch, *A new tool for combustion research a quartz piston engine*, Report, SAE Technical Paper, 1961.

[65] H. A. Michelsen, "Understanding and predicting the temporal response of laser-induced incandescence from carbonaceous particles", *The journal of chemical physics* **118**, 15 (2003), pp. 7012–7045.

[66] R. P. C. Zegers et al., "Pre- and post-injection flow characterization in a heavy-duty diesel engine using high-speed PIV", *Experiments in fluids* **53**, 3 (2012), pp. 731–746.

[67] H. Bladh and P.-E. Bengtsson, "Characteristics of laser-induced incandescence from soot in studies of a time-dependent heat-and mass-transfer model", *Applied physics b* **78**, 2 (2004), pp. 241–248.

Appendix A

MCP Gain Satturation

In this appendix, the MCP gain equation and recovery, used in Chapter 2, is derived, based on a TLM-model. Another version of this derivation can also be found in [17]. However, the derivation presented here is better adapted to the application presented in the thesis, aimed at experimentally characterizing the charge depletion that occurs in an image intensifier.

On the basis of Eq. (2.2) and Eq. (2.4) the following equations can be derived:

$$I(z,t) + i_c(z,t) + i(z,t) = F(t), \tag{A.1a}$$

$$\frac{1}{r}\frac{\partial \phi(z,t)}{\partial z} = I(z,t), \tag{A.1b}$$

$$\frac{1}{h}\frac{\partial}{\partial t}\left(\frac{\partial \phi(z,t)}{\partial z}\right) = i_c(z,t), \tag{A.1c}$$

$$\frac{1}{i(z,t)}\frac{\partial i(z,t)}{\partial z} = k\ln\frac{V_s}{V_m} + k\ln\left(1 + \frac{L}{V_s}\frac{\partial \phi(z,t)}{\partial z}\right). \tag{A.1d}$$

Equation (A.1a) shows that the sum of all currents is independent on the position along the MCP tubes. Equations (A.1b), (A.1c) and (A.1d) express the resistive current that is in excess of the nominal strip current, the inductive current and the incremental amplification of the signal current, respectively.

We are seeking a function that translates the amplified signal into the initial signal. We call this the inverse gain and define it as $g^{-1}(z,t) = {}^{i(z,t)}/_{i_L(t)}$, where $i_L(t) = i(L,t)$ is the signal current at the end of the MCP. By substituting this into Eq. (A.1d), we obtain

$$\frac{1}{g^{-1}(z,t)}\frac{\partial g^{-1}(z,t)}{\partial z} = k\ln\frac{V_s}{V_m} + k\ln\left(1 + \frac{L}{V_s}\frac{\partial \phi(z,t)}{\partial z}\right), \tag{A.2}$$

which after integration between z and L becomes

$$g^{-1}(z,t) = \exp\left[k\ln\left(\frac{V_s}{V_m}\right)(z-L) + k\int_z^L \ln\left(1 + \frac{L}{V_s}\frac{\partial \phi(z',t)}{\partial z'}\right)dz'\right]. \tag{A.3}$$

The integral in Eq. (A.3) correspond to the perturbed part of the gain. Thus, we define $G \equiv k \ln\left({}^{V_s}/_{V_m}\right)$, and call it the logarithmic gain. In the unperturbed case the signal in the MCP is amplified according to $i(z,t) = i_L(t)\mathrm{e}^{G(L-z)}$.

To find a solution for the quantity ${}^{\partial\phi(z,t)}/_{\partial z}$ on the right hand side of Eq. (A.3) we add Eq. (A.1c) to Eq. (A.1b)

$$\frac{1}{r}\frac{\partial\phi(z,t)}{\partial z} + \frac{1}{h}\frac{\partial}{\partial t}\left(\frac{\partial\phi(z,t)}{\partial z}\right) = I(z,t) + i_c(z,t). \tag{A.4}$$

The right hand side of Eq. (A.4) is the current in the channel wall in excess of the nominal strip current, termed here the excess wall current.

$$I(z,t) + i_c(z,t) = i_w(z,t) \tag{A.5}$$

Thus, by rearranging Eq. (A.4) and using the fact that ${}^{h}/_{r} = {}^{1}/_{RC}$ one obtains

$$\frac{\partial}{\partial t}\left(\frac{\partial\phi(z,t)}{\partial z}\right) = h i_w(z,t) - \frac{1}{RC}\frac{\partial\phi(z,t)}{\partial z}, \tag{A.6}$$

which can be solved for by multiplying by $\mathrm{e}^{t/RC}$ and integrating over t.

$$\frac{\partial\phi(z,t)}{\partial z} = \mathrm{e}^{-t/RC}\left[\frac{\partial\phi(z,0)}{\partial z} + h\int_0^t \mathrm{e}^{t'/RC} i_w(z,t')dt'\right]. \tag{A.7}$$

For a short pulse where $t << RC$, $\mathrm{e}^{t/RC} \approx \mathrm{e}^{-t/RC} \approx 1$, Eq. (A.7) can be simplified to

$$\frac{\partial\phi(z,t)}{\partial z} = \frac{\partial\phi(z,0)}{\partial z} + h\int_0^t i_w(z,t')dt'. \tag{A.8}$$

Combining Eq. (A.8) with Eq. (A.3) yields

$$g^{-1}(z,t) = \ldots$$
$$\exp\left[G(z-L) + k\int_z^L \ln\left(1 + \frac{L}{V_s}\left(\frac{\partial\phi(z',0)}{\partial z} + h\int_0^t i_w(z',t')dt'\right)\right)dz'\right]. \tag{A.9}$$

Since the sum of currents, as expressed in Eq. (A.1a), is independent of position, one can express the currents in the integral on the right hand side of Eq. (A.9) as

$$i_w(z,t) = i_{wL}(t) + i_L(t) - i(z,t), \tag{A.10}$$

where $i_{wL}(t) = i(L,t)$. Thus, the last integral in Eq. (A.9) can be expressed as

$$\int_0^t i_w(z,t')dt' = \int_0^t \left(i_{wL}(t') + i_L(t')\right)dt' - \int_0^t i(z,t')dt', \tag{A.11}$$

where the answer to the first integral on the right hand side can be found by integrating Eq. (A.8) over z

$$\phi(z,t) = \phi(z,0) + h\left(z\int_0^t i_{wL}(t') + i_L(t')dt' - \int_0^z\int_0^t i(z',t')dt'dz'\right). \tag{A.12}$$

At the limits of the MCP, i.e. at $z = 0$ and $z = L$, the voltage is defined by the external voltage and consequently $\phi(0,t) = \phi(L,t) = 0$. Thus, inserting $z = L$ into Eq. (A.12) and combining that with Eq. (A.11) one finds that

$$\int_0^t i_w(z,t')dt' = \frac{1}{L}\int_0^L \int_0^t i(z,t')dt'dz - \int_0^t i(z,t')dt'. \tag{A.13}$$

Remembering that $g^{-1}(z,t) = {}^{i(z,t)}/_{i_L}(t)$, Eq. (A.13) can now be written as

$$\int_0^t i_w(z,t')dt' = \frac{1}{L}\int_0^L \int_0^t g^{-1}(z,t')i_L(t')dt'dz - \int_0^t g^{-1}(z,t')i_L(t')dt'. \tag{A.14}$$

Inserted in Eq. (A.9) this yields

$$\begin{aligned} g^{-1}(z,t) = \exp\Bigg[G(z-L) + k\int_z^L \ln\Bigg(1 + \frac{L}{V_s}\frac{\partial\phi(z',0)}{\partial z} + \dots \\ \frac{h}{L}\int_0^L \int_0^t g^{-1}(z,t')i_L(t')dt'dz - h\int_0^t g^{-1}(z',t')i_L(t')dt'\Bigg)dz'\Bigg]. \end{aligned} \tag{A.15}$$

From Eq. (A.15) it is evident that $g^{-1}(z,t)$ appear on both sides of the equal sign. However, since the the integral on the right hand side of Eq. (A.15) represents a perturbation of the ideal undepleted gain, the equation can be solved numerically in an iterative manner. First, the unperturbed gain is calculated and is inserted on the right side of Eq. (A.15). A first approximation of the perturbed gain is thus obtained, one that is used to calculate a second, refined version. This procedure is continued until the calculations converge.

Prior to the first exposure, the electric field is unperturbed and the quantity ${}^{\partial\phi(z',0)}/_{\partial z}$ can be set to zero. At the end of the first pulse, the electric field has become perturbed according to Eq. (A.8). If the MCP is exposed again before the gain has recovered its initial state, the perturbed part of the electric field will be nonzero and needs to be calculated.

The recovery of the electric field is given by Eq. (A.7), but with $\phi(z,0)$ referring here to the excess voltage just after the first exposure, i.e. the beginning of the recovery phase. Since the sum of currents is independent of z according to Eq. (A.1a) and the signal is absent during the recovery phase the excess wall current is also independent of z. Thus, $i_w(z,t) = i_w(0,t)$ and Eq. (A.7) can be written as

$$\frac{\partial\phi(z,t)}{\partial z} = \mathrm{e}^{-t/RC}\left[\frac{\partial\phi(z,0)}{\partial z} + h\int_0^t \mathrm{e}^{t'/RC} i_w(0,t')dt'\right]. \tag{A.16}$$

Integrating Eq. (A.16) over z gives

$$\phi(z,t) = \mathrm{e}^{-t/RC}\left[\phi(z,0) + hz\int_0^t \mathrm{e}^{t'/RC} i_w(0,t')dt'\right]. \tag{A.17}$$

With the boundary condition $\phi(0,t) = \phi(L,t) = 0$, Eq. (A.17) with $z = L$ becomes

$$hL \int_0^t \mathrm{e}^{t'/RC} i_w(0,t')dt' = 0. \tag{A.18}$$

Thus, the recovery of the excess electric field can be simplified (from Eqs. (A.16) and (A.18)) to

$$\frac{\partial\phi(z,t)}{\partial z} = \frac{\partial\phi(z,0)}{\partial z}\mathrm{e}^{-t/RC}. \tag{A.19}$$

Summary of Papers

Paper I: A method to extend time-resolved planar-laser-induced measurements to the third dimension by scanning the laser sheet is demonstrated. The method is applied to a water droplet flow from which Mie scattered light is recorded.

I planned and executed the experiments and the post processing of the data. I was responsible for writing the paper.

Paper II: The method developed in Paper I was extended here to PLIF. The flame fronts and concentration of OH in a flame were resolved in time and in the three spatial dimensions.

I planned and executed the experiments and the post processing of the data. I was responsible for writing the paper.

Paper III: An experimental and analytical method that compensates for MS, signal attenuation and laser extinction is demonstrated. The method is demonstrated on a cuvette of known particle distribution and on a water spray.

I took part of the planning and execution of the experiments. I did the post-processing of the data and was responsible for writing the paper.

Paper IV: High repetition rate imaging was conducted on laser light scattered on droplets in a Diesel spray injected in a light-duty Diesel engine. The penetration length for early injections was studied for different injection strategies.

I took part in the planning and was responsible for the laser and imaging part of the experimental work. I performed the image analysis and aided in the writing of the paper.

Paper V: The soot distribution in a heavy duty engine was followed in time by means of high speed LII. The applicability of the technique under such conditions was investigated.

I took part in the experiments conducted in the engine and aided in the data analysis and writing of the paper.

Paper VI: The impact on the soot distribution of the oxygen concentration was measured in a heavy duty diesel engine by means of high speed LII. The results

indicate soot oxidation to be more important than soot formation for the engine-out soot.

I took part in the experiments conducted in the engine and had a minor role in the data analysis and writing of the paper.

Paper VII: The flame jet propagation in a pre-chamber-ignited large-bore gas engine was investigated by means of fuel tracer LIF.

I took part in the planning of the experiments and was responsible for the optical diagnostics part of the experiment. I was responsible for the data analysis, except for the heat release analysis. I was responsible for writing the paper.